

Bayesian analysis of a (3+1)D hybrid approach with initial conditions from hadronic transport

Niklas Götz^{1,2}, Iurii Karpenko³ and Hannah Elfner^{4,1,2,5}

¹*Goethe University Frankfurt, Department of Physics,*

Institute for Theoretical Physics, 60438 Frankfurt, Germany

²*Frankfurt Institute for Advanced Studies, 60438 Frankfurt am Main, Germany*

³*Faculty of Nuclear Sciences and Physical Engineering,*

Czech Technical University in Prague, 11519 Prague 1, Czech Republic

⁴*GSI Helmholtzzentrum für Schwerionenforschung, 64291 Darmstadt, Germany and*

⁵*Helmholtz Research Academy Hesse for FAIR (HFHF), GSI Helmholtz Center,*

Campus Frankfurt, 60438 Frankfurt am Main, Germany

(Dated: March 14, 2025)

Background: The SMASH-vHLLC-hybrid model integrates the SMASH transport code for the hadronic phase and the vHLLC hydrodynamic model for the QGP phase in heavy-ion collisions. Bayesian analysis offers a robust statistical method to constrain model parameters of a hybrid approach and evaluate uncertainties by comparing predictions with experimental data. Traditional modelling often relies on parametric assumptions for initial conditions, which may limit the ability to constrain the parameter space due to overfitting.

Purpose: This study aims to apply statistical learning, specifically Bayesian inference, to the (3+1)D SMASH-vHLLC-hybrid model using initial conditions generated by the SMASH transport code itself, with the objective of constraining model parameters and gaining deeper insight on the temperature and baryochemical potential dependence of both the shear and the bulk viscosity.

Method: This study is performed in the hybrid approach SMASH-vHLLC, composed of the hadronic transport approach SMASH and the (3+1)D viscous hydrodynamic code vHLLC. A Bayesian framework is employed, utilising Markov Chain Monte Carlo (MCMC) sampling to explore the parameter space. The analysis compares model predictions against experimental observables, including particle yields, momentum and flow coefficients both at midrapidity as well as in forward and backward direction.

Results: We find that the SMASH-vHLLC-hybrid framework, using hadronic initial conditions for Au+Au collisions at different beam energies, can reproduce a variety of experimental observables at midrapidity and forward/backward rapidities. Notably, the preferred posterior distribution suggests a near-vanishing specific shear viscosity in the high-temperature QGP phase, combined with moderate-to-large bulk viscosity around the phase transition region, although the constraints on baryochemical potential dependence are weak.

Conclusions: Our findings reveal that a hadronic initial condition constrains the evolution more strictly at intermediate energies, making parameters such as the hydrodynamic onset time highly sensitive. Intriguingly, the extracted shear viscosity differs substantially from previous Bayesian analyses, motivating further systematic studies with higher-statistics data sets and refined modeling assumptions.

I. INTRODUCTION

The study of Quark-Gluon Plasma (QGP) characterization has remained a central focus in high-energy nuclear physics, particularly within the experimental frameworks provided by facilities such as the Relativistic Heavy Ion Collider (RHIC) at Brookhaven National Laboratory and the Large Hadron Collider (LHC) at CERN [1, 2]. These experiments enable a detailed exploration of the QGP, a state of matter where quarks and gluons, the fundamental constituents of protons and neutrons, are deconfined due to extreme temperatures and densities. A crucial component of this investigation is the RHIC Beam Energy Scan (BES) program, which systematically varies the center-of-mass energy of colliding ions to probe the QCD phase diagram over a wide range of temperature and baryon chemical potential [3–6]. The BES pro-

gram is particularly significant as it seeks to identify the transition between hadronic matter and the QGP, and to locate a potential critical point and first-order phase boundaries within the QCD phase diagram, thereby offering insights into the emergent properties of the strong nuclear force [7–10].

Theoretical descriptions of QGP evolution in relativistic heavy-ion collisions are complex, multifaceted and computationally expensive. Relevant length scales change dynamically as the collision systems evolve. Therefore, it is necessary to match different types of physical models in a multi-stage approach. They typically involve a combination of relativistic viscous hydrodynamics as an effective long-wavelength description of the collective behavior and hadronic transport models [11–23]. Despite the success of these models in describing collective QGP behavior, significant uncertainties persist, particu-

larly in the initial conditions and the transport properties of the medium. These uncertainties must be quantified to extract precise information about QGP properties, such as shear and bulk viscosities [24–29].

It is challenging to compute the QGP transport coefficients from first principles [30]. There have been several attempts using lattice QCD techniques to compute the plasma’s shear viscosity for a pure gluon system [31–34]. On the other hand, extensive phenomenological studies were able to show that the hadronic observables measured from heavy-ion collisions are sensitive to the viscosities in the QGP [14, 24, 35–39]. There have been many studies using hydrodynamics in heavy-ion collision simulations to estimate the specific shear viscosity η/s for the QGP [24, 35, 40–42].

Similarly, due to the extremely short lifetime, the initial state of heavy ion collisions is experimentally not accessible, leading to a variety of initial state models to exist [12, 43–57]. Relativistic viscous hydrodynamics transforms the initial-state spatial inhomogeneities to anisotropies in the final-state hadrons momentum distributions. This theoretical description allows us to access information about the initial conditions of heavy-ion collisions and transport properties of the QGP from the experimental measurements. As many initial state models are motivated by physics but still rich in tunable parameters, and as final state anisotropies are both sensitive to the initial state inhomogeneities and to the viscosities, it is highly desirable to use initial state models with a minimal set of parameters.

An example for an approach using such an initial condition is SMASH-vHLLC-hybrid, which uses hadronic transport both for the late stage rescattering, but also to generate the initial energy and charge density [12]. It has access to the full (3+1)D evolution and information about initial state transverse momentum, which has been shown to be relevant especially for the flow of central collisions [58]. Additionally, due to conservation of all charges and the successful reproduction of experimental results across a wide range of collision energies, it allows for the study of temperature and baryochemical dependent viscosities [59].

Recent efforts to determine the QGP’s transport coefficients have focused on Bayesian inference techniques, which offer a robust framework for constraining these properties by integrating experimental data with theoretical models [60–71]. These studies have significantly advanced our understanding of QGP properties, particularly by incorporating the temperature and baryon chemical potential dependence of the specific shear and bulk viscosities into high-dimensional model parameter spaces. Nevertheless, the uncertainties remain substantial.

To leverage the extensive data from RHIC BES, we conduct comprehensive modeling of (3+1)D QGP dynamics within a 15-dimensional model parameter space, utilizing state-of-the-art relativistic viscous hydrodynamics and hadronic transport simulations. This is both a

considerably smaller parameter space than current efforts [72, 73] as well as larger than earlier works, such as Ref. [62], which explored a much smaller five-dimensional parameter space. Due to the considerably decreased number of parameters for the initial condition, we can instead focus on a more complete study of the functional form of viscosities.

In this work, we build upon these developments by performing a systematic Bayesian inference analysis of RHIC BES measurements using full (3+1)D event-by-event simulations. Following the insights into the performance of different emulation strategies, we employ state-of-the-art Gaussian Process model emulators, enhancing the precision of our predictions [74]. This analysis will report and analyze the posterior distribution for all model parameters, providing a thorough investigation of the QGP’s transport coefficients. The results will include a detailed sensitivity analysis between model parameters and experimental observables, shedding light on the intricate dependencies that govern QGP behavior in relativistic heavy-ion collisions.

This work is structured as follows: In section II, the hybrid approach SMASH-vHLLC-hybrid, within which this study is performed, is briefly summarized. Section III demonstrates the choice of the parameterisation of the viscosities, as well as the choice of systems and observables. In section IV, an outline is given of the setup of the Bayesian analysis employed in this study. Lastly, section VI demonstrates the sensitivity of different parameters to experimental observables, and shows the posterior distribution of optimal parameters, depending on the set of experimental data. From the MAP predictions, we validate that we can successfully reproduce experimental data. To conclude, a brief summary and outlook can be found in section VII.

II. MODEL DESCRIPTION

The theoretical calculations presented in this work utilize the SMASH-vHLLC-hybrid approach [75], a publicly available framework designed for the theoretical study of heavy-ion collisions within the energy range of $\sqrt{s_{NN}} = 4.3$ GeV to $\sqrt{s_{NN}} = 5.02$ TeV. The SMASH-vHLLC-hybrid model has demonstrated robust agreement with experimental data across a broad spectrum of collision energies while ensuring the conservation of all conserved charges (B, Q, S). It is particularly effective in capturing longitudinal baryon dynamics at intermediate collision energies [12], which motivated its development.

A concise overview of the model’s components is provided below. For more detailed descriptions, readers are referred to [12].

A. Initial Conditions

The input to the fluid-dynamic evolution is the initial condition, which characterizes the system's evolution prior to the onset of hydrodynamic applicability. SMASH generates these initial conditions by simulating the interactions of particles from the colliding nuclei until each particle reaches a fixed proper time τ_0 . At this point, the particle is removed from the simulation. This process continues until all particles reach a hypersurface of constant proper time τ_0 . The transition from Cartesian coordinates (used by SMASH) to Milne coordinates (used for hydrodynamic evolution) necessitates this procedure. In this work, we investigate the optimal value for τ_0 proportional to the passing time of the nuclei, $\tau_{0,\text{pass}}$:

$$\tau_{0,\text{pass}} = \frac{R_P + R_T}{\sqrt{\left(\frac{\sqrt{s_{NN}}}{2m_N}\right)^2 - 1}}, \quad (1)$$

where R_P and R_T are the radii of the projectile and target nuclei, respectively, $\sqrt{s_{NN}}$ is the collision energy, and m_N is the nucleon mass.

To initialize the hydrodynamic evolution, the energy-momentum and charge depositions from the particles crossing the iso- τ hypersurface are smoothed to prevent shock waves. A Gaussian smearing kernel [21] is applied, with parameters obtained from [12]. These parameters are critical for tuning the initial conditions to match experimental data, as demonstrated in similar studies [76]. Notably, this approach requires only three parameters to define the initial conditions.

B. Hydrodynamic Evolution

The 3+1D viscous hydrodynamics code vHLLE [77] is used to simulate the evolution of the hot and dense fireball. It solves the following hydrodynamic equations:

$$\partial_\nu T^{\mu\nu} = 0, \quad (2)$$

$$\partial_\nu j_B^\nu = 0, \quad \partial_\nu j_Q^\nu = 0, \quad \partial_\nu j_S^\nu = 0, \quad (3)$$

which describe the conservation of energy, momentum, net-baryon number, net-charge, and net-strangeness. The energy-momentum tensor is decomposed as:

$$T^{\mu\nu} = \epsilon u^\mu u^\nu - \Delta^{\mu\nu}(p + \Pi) + \pi^{\mu\nu}, \quad (4)$$

where ϵ is the local rest frame energy density, p is the equilibrium pressure, Π is the bulk pressure, and $\pi^{\mu\nu}$ represents the shear stress tensor. These equations are solved using the second-order Israel-Stewart formalism [78, 79].

At this stage, particles are converted into fluid elements, which evolve based on a chiral mean-field equation of state [80–82], matched to a hadron resonance gas

at lower energy densities. While derived from the parity doublet model, the equation of state aligns well with lattice QCD predictions and constraints from astrophysics. Evolution continues until the energy density reaches a switching value, a technical parameter optimized in this work. The freeze-out hypersurface is then constructed using the CORNELIUS subroutine [83], and thermodynamic properties are calculated using the SMASH hadron resonance gas equation of state [12] to ensure continuity of energy-momentum flow through the hypersurface.

C. Particle Sampler

To transition from fluid elements to particles, the SMASH-vHLLE hybrid approach employs the SMASH-hadron-sampler [84]. This sampler uses the grand-canonical ensemble to particlize each surface element independently. Hadrons are sampled based on a Poisson distribution, with the mean set to the thermal multiplicity. Momenta are sampled according to the Cooper-Frye formula [85]. Corrections to the distribution function δf_{visc} due to finite shear and bulk viscosity are incorporated using the Grad's 14-moment ansatz, assuming uniform corrections across all hadron species and neglecting charge diffusion. These corrections depend implicitly on the temperature (T) and baryochemical potential (μ_B). The result is a particle list compatible with SMASH, enabling subsequent evolution. A comprehensive description of the sampling procedure is available in [21].

D. Hadronic Transport

The SMASH model [86–88] solves the relativistic Boltzmann equation by modeling the collision integral through the formation, decay, and scattering of hadronic resonances. The model includes all hadrons listed by the Particle Data Group (PDG) up to a mass of 2.35 GeV [89]. Initial nucleon-nucleon, as well as other hard scatterings are handled by Pythia 8 [90], while soft interactions use a string model. For these calculations, the SMASH version 3.1 was utilized.

As the system expands, cools down and converts to hadronic phase, the Boltzmann equation with hadronic DOF becomes applicable. At the same time, as the mean free path becomes longer, the applicability of medium (fluid) picture gradually ceases. SMASH handles hadronic rescatterings and resonance decays that happen after the particlization hypersurface. In order to do that, it propagates the input hadrons back to a common starting time and assigns appropriate formation times so that the hadrons are only allowed to interact or decay beyond the particlization surface. As the hadronic system expands further, the mean distance between the hadrons grows such that the interactions gradually cease.

In the fluid approximation, viscosities of the medium are essentially input parameters to the modelling. Differ-

ent from that, in the hadronic phase, the viscosities are determined by the cross sections, which we consider as fixed. Therefore, it is inaccessible to the Bayesian Analysis which follows.

III. SETUP

This section outlines the essential prerequisites for conducting a Bayesian analysis, focusing on the selection of input parameter ranges and their parameterization. The setup ensures a comprehensive exploration of the model's predictive capabilities across key aspects of the QCD phase diagram.

A. Priors and Parameterization

We consider prior distributions for three distinct parameter groups: (1) technical parameters defining the interfaces between the different stages of the hybrid approach, (2) parameters for shear viscosity, and (3) parameters for bulk viscosity. Each parameter set is discussed in detail below.

1. Technical Parameters

The technical parameters govern the interaction between the initial hadronic transport stage and the subsequent hydrodynamic evolution. These include two smearing parameters: R_{\perp} , for transverse smearing, and R_{η} , for longitudinal smearing. For the original definition of SMASH-vHLL-*Hybrid*, these parameters were energy-dependent to match experimental data. However, in this study, we absorb all collision energy dependence into the temperature and baryochemical potential dependencies of viscosities. As such, R_{\perp} and R_{η} are treated as constants within the range $[0.2, 2.2]$ fm and $[0.2, 3.0]$, respectively. The lower limit reflects finite grid resolution constraints, while the upper limit avoids excessive smoothing, which could erase essential fluctuations.

The initialization time, τ_0 , is chosen proportional to the passing time of the nuclei. We assume that hydrodynamic evolution should begin only after the nuclei have passed in order for all participant scatterings to contribute to the medium production. However, τ_0 must remain significantly shorter than the system's evolution time to capture relevant dynamics. Accordingly, the proportionality factor is selected within the range $[0.8, 2.5]$.

The switching energy density, ϵ_{switch} , marks the transition from hydrodynamics to transport. It must represent a regime where both descriptions are approximately valid—neither too dilute for hydrodynamics nor too dense for transport. This parameter is constrained to $[0.25, 0.75] \frac{\text{GeV}}{\text{fm}^3}$. Table I summarizes the prior ranges for all technical parameters.

Parameter		
R_{\perp}	$[0.2, 2.2]$	fm
R_{η}	$[0.2, 3.0]$	fm
$\tau_{\text{IC, scale}}$	$[0.8, 2.5]$	
ϵ_{switch}	$[0.25, 0.75]$	$\frac{\text{GeV}}{\text{fm}^3}$

TABLE I. Priors for technical parameters.

2. Shear Viscosity

The shear viscosity parameterization accounts for temperature and baryochemical potential dependence:

$$\frac{\eta T}{\epsilon + P} = \max \left(0, (\eta/s)_{\text{kink}} + \begin{cases} a_{l,\eta}(T - T_c) & T < T_c, \\ a_{h,\eta}(T - T_c) & T > T_c \end{cases} \right) \times \left(1 + a_{\mu_B} \frac{\mu_B}{\mu_{B,0}} \right), \quad (5)$$

$$T_c = T_{\eta,0} + b_{\mu_B} \frac{\mu_B}{\mu_{B,0}}. \quad (6)$$

The parameters are illustrated in fig. 1. The parameter $(\eta/s)_{\text{min}}$ sets the shear viscosity at T_c for $\mu_B = 0$, with $a_{l,\eta}$ and $a_{h,\eta}$ controlling the slopes in the low- and high-temperature regions, respectively. The critical temperature T_c varies with μ_B , governed by $T_{\eta,0}$ and b_{μ_B} . The overall viscosity is scaled by a_{μ_B} to reflect μ_B -dependent effects.

This flexible structure accommodates a temperature dependence consistent with earlier studies [65, 66], while explicitly incorporating μ_B effects. We allow for an explicit temperature dependence, greatly increasing the flexibility with respect to [73] which featured only mild, linear temperature dependence. This allows us to test whether earlier agreements with constant, temperature independent shear viscosity holds in our model as well [66].

The prior ranges (table II) are broad enough to include both μ_B -independent and constant shear viscosities. The KSS-bound of 0.08 is not enforced, allowing the analysis to explore the parameter space freely.

Parameter	
$a_{l,\eta}$	$[-15, 1]$
$a_{h,\eta}$	$[-15, 1.75]$
$T_{\eta,0}$	$[0.09, 0.25]$ GeV
$(\eta/s)_{\text{min}}$	$[0.001, 0.35]$
a_{μ_B}	$[-0.8, 7]$
b_{μ_B}	$[-0.3, 0.8]$

TABLE II. Priors for shear viscosity parameters.

3. Bulk Viscosity

In contrast to recent studies [73] we choose one bulk viscosity parameterization for all collision energies. The

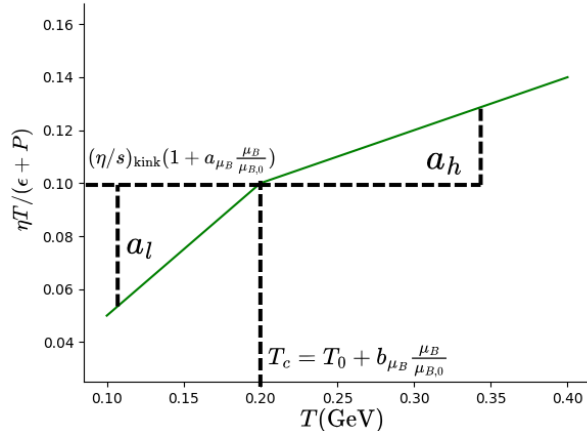


FIG. 1. Illustration of the shear viscosity parameterization.

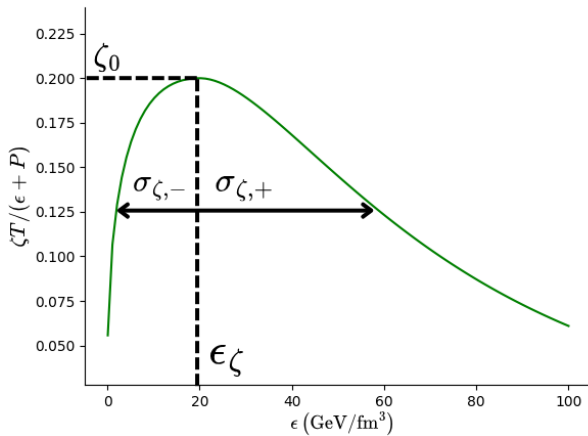


FIG. 2. Illustration of the bulk viscosity parameterization.

bulk viscosity parameterization incorporates μ_B implicitly by depending on the energy density ϵ . This approach assumes that the bulk viscosity peak follows a line of constant ϵ , potentially aligning with the QCD phase crossover at finite μ_B . The parameterization is:

$$\frac{\zeta T}{\epsilon + P} = \zeta_0 \begin{cases} \exp\left(-\beta \frac{(\epsilon^{1/4} - \epsilon_\zeta^{1/4})^2}{2\sigma_{\zeta,-}^2}\right), & \epsilon < \epsilon_\zeta, \\ \exp\left(-\beta \frac{(\epsilon^{1/4} - \epsilon_\zeta^{1/4})^2}{2\sigma_{\zeta,+}^2}\right), & \epsilon > \epsilon_\zeta, \end{cases} \quad (7)$$

where ζ_0 controls the peak amplitude, ϵ_ζ sets the location of the peak, and $\sigma_{\zeta,-}$ and $\sigma_{\zeta,+}$ define the widths below and above ϵ_ζ , respectively. As we want to have a similar shape than comparable parameterization in the temperature, we take the fourth root of the energy density and scale it by a conversion factor. Figure 2 illustrates this parameterization, while table III lists the prior ranges.

Parameter		
ζ_0	[0, 0.2]	
ϵ_ζ	[0.5, 40]	$\frac{\text{GeV}}{\text{fm}^3}$
$\sigma_{\zeta,-}$	[0.005, 0.1]	
$\sigma_{\zeta,+}$	[0.01, 0.15]	

TABLE III. Priors for bulk viscosity parameters.

B. Systems

We investigate three collision energies—7.7 GeV, 19.6 GeV, and 200 GeV—spanning a broad region of the QCD phase diagram. To optimize computational efficiency, we limit the analysis to three centrality classes: 0–5% (central), 15–25% (only for rapidity-dependent data at 200 GeV), and 20–30% (mid-central). This selection captures key dynamics while reducing computational costs. The underlying assumption is that a model which successfully describes two centrality classes is also able to describe all other classes.

These systems provide a wide μ_B coverage of mean values of around 0 to 400 MeV at freeze-out [91–93], offering insights into μ_B -dependent effects. Observables sensitive to longitudinal dynamics further enhance this range [94].

C. Observables

Table IV summarizes the experimental observables. They consist of STAR RHIC BES data integrated bulk, enriched with $dN/d\eta$ from PHOBOS at $\sqrt{s_{NN}} = 200$ GeV. For 19.6 GeV, there is a choice between $dN/d\eta$ data from PHOBOS and STAR, which show substantial differences [95]. We chose the more recent STAR data for our tuning. η -differential data is included until a cutoff of 3 in forward and backwards-rapidity. The total dataset size is 168 datapoints.

For the identified particle observables, we have excluded antiprotons due to the high statistical uncertainties. Additionally, the initialisation with hadronic transport leads to excess baryon charge at 200 GeV, due to which we have excluded protons at 200 GeV [96].

IV. METHOD

This section describes the methodology employed to perform Bayesian parameter inference within the SMASH-vHLLH-hybrid framework, encompassing parameter sampling, emulation, and posterior distribution estimation.

A. Parameter Sampling and Event Generation

To explore the 15-dimensional parameter space, we employ Latin Hypercube Sampling (LHS), implemented

$\sqrt{s_{NN}}$	0-5%	15-25%	20-30%
200 GeV	$dN/dy _{y=0}(\pi^{+,-}, K^{+,-})$ [97] $\langle p_T \rangle _{y=0}(\pi^{+,-}, K^{+,-})$ [97] $v_2^{\text{ch}}\{2\} _{y=0}$ [98], $v_3^{\text{ch}}\{2\} _{y=0}$ [99] $dN^{\text{ch}}/d\eta$ [100], $v_2^{\text{ch}}(\eta)$ [101]	$dN^{\text{ch}}/d\eta$ [100], $v_2^{\text{ch}}(\eta)$ [101]	$dN/dy _{y=0}(\pi^{+,-}, K^{+,-})$ [97] $\langle p_T \rangle _{y=0}(\pi^{+,-}, K^{+,-})$ [97] $v_2^{\text{ch}}\{2\} _{y=0}$ [98], $v_3^{\text{ch}}\{2\} _{y=0}$ [99]
19.6 GeV	$dN/dy _{y=0}(\pi^{+,-}, K^{+,-}, p)$ [93] $\langle p_T \rangle _{y=0}(\pi^{+,-}, K^{+,-}, p)$ [93] $dN^{\text{ch}}/d\eta$ [95] $v_2^{\text{ch}}\{2\} _{y=0}$ [98], $v_3^{\text{ch}}\{2\} _{y=0}$ [99]		$dN/dy _{y=0}(\pi^{+,-}, K^{+,-}, p)$ [93] $\langle p_T \rangle _{y=0}(\pi^{+,-}, K^{+,-}, p)$ [93] $dN^{\text{ch}}/d\eta$ [95] $v_2^{\text{ch}}\{2\} _{y=0}$ [98], $v_3^{\text{ch}}\{2\} _{y=0}$ [99]
7.7 GeV	$dN/dy _{y=0}(\pi^{+,-}, K^{+,-}, p)$ [93] $\langle p_T \rangle _{y=0}(\pi^{+,-}, K^{+,-}, p)$ [93] $v_2^{\text{ch}}\{2\} _{y=0}$ [98], $v_3^{\text{ch}}\{2\} _{y=0}$ [99]		$dN/dy _{y=0}(\pi^{+,-}, K^{+,-}, p)$ [93] $\langle p_T \rangle _{y=0}(\pi^{+,-}, K^{+,-}, p)$ [93] $v_2^{\text{ch}}\{2\} _{y=0}$ [98], $v_3^{\text{ch}}\{2\} _{y=0}$ [99]

TABLE IV. The experimental measurements in Au+Au collisions used in this Bayesian inference study.

via pyDOE [102, 103] and included in SMASH-vHLLH-Hybrid [75]. This method ensures an efficient and uniform coverage of the prior space. A total of 750 parameter points are sampled, and for each, we generate 250 events per centrality class.

The centrality classes are selected by generating 5000 initial state events, sorting them by energy content, and selecting events accordingly. To achieve equal statistics for all centrality classes, only half of the events are chosen for the wider classes. These initial events are propagated through all stages of the hybrid approach. To improve statistical accuracy and maintain charge conservation, oversampling is performed at different magnitudes depending on the collision energy: 4000, 2000, and 500 events for $\sqrt{s_{NN}} = 7.7, 19.6,$ and 200 GeV, respectively.

B. Observable Analysis

Analysis of the generated events is conducted using the SPARKX Python package in version 2.0.2 [104, 105], which automates the computation of bulk observables and flow coefficients. This reliable and efficient framework facilitates a direct comparison between model predictions and experimental data.

C. Bayesian Framework

The primary goal of the Bayesian analysis is to identify the optimal parameter set within the prior range such

that the model predictions closely match experimental data. Let $\boldsymbol{\theta} \equiv (\theta_1, \dots, \theta_m)$ represent the model parameters, and let $\mathbf{y}_{\text{sim}}(\boldsymbol{\theta})$ denote the simulation output in \mathbb{R}^d , where d is the dimension of the observable space. These outputs are compared to the experimental values $\mathbf{y}_{\text{exp}} \equiv (y_{\text{exp},1}, \dots, y_{\text{exp},d})$, forming a statistical model:

$$\mathbf{y}_{\text{exp}} = \mathbf{y}_{\text{sim}}(\boldsymbol{\theta}) + \boldsymbol{\epsilon}, \quad (8)$$

where $\boldsymbol{\epsilon}$ is the residual error, assumed to follow a multivariate normal (MVN) distribution with mean $\mathbf{0}$ and covariance $\boldsymbol{\Sigma}$.

The Bayesian framework updates prior beliefs about the parameters $\boldsymbol{\theta}$ using Bayes' theorem:

$$\mathcal{P}(\boldsymbol{\theta}|\mathbf{y}_{\text{exp}}) = \frac{\mathcal{P}(\mathbf{y}_{\text{exp}}|\boldsymbol{\theta})\mathcal{P}(\boldsymbol{\theta})}{\mathcal{P}(\mathbf{y}_{\text{exp}})}. \quad (9)$$

Here, $\mathcal{P}(\boldsymbol{\theta}|\mathbf{y}_{\text{exp}})$ is the posterior probability density, $\mathcal{P}(\boldsymbol{\theta})$ is the prior, $\mathcal{P}(\mathbf{y}_{\text{exp}})$ is the evidence, and $\mathcal{P}(\mathbf{y}_{\text{exp}}|\boldsymbol{\theta})$ is the likelihood. Given the MVN assumption for $\boldsymbol{\epsilon}$, the likelihood is expressed as:

$$\mathcal{P}(\mathbf{y}_{\text{exp}}|\boldsymbol{\theta}) = \frac{1}{\sqrt{|2\pi\boldsymbol{\Sigma}|}} \exp\left[-\frac{1}{2}(\mathbf{y}_{\text{sim}}(\boldsymbol{\theta}) - \mathbf{y}_{\text{exp}})^\top \boldsymbol{\Sigma}^{-1}(\mathbf{y}_{\text{sim}}(\boldsymbol{\theta}) - \mathbf{y}_{\text{exp}})\right]. \quad (10)$$

D. Gaussian Process Emulation

Direct evaluation of eq. (9) is computationally expensive, as simulating each parameter set requires significant

computational resources. We want therefore to minimise the number of parameter sets to be evaluated while at the same time minimise the loss of information. In order to achieve this, we employ Gaussian Process (GP)

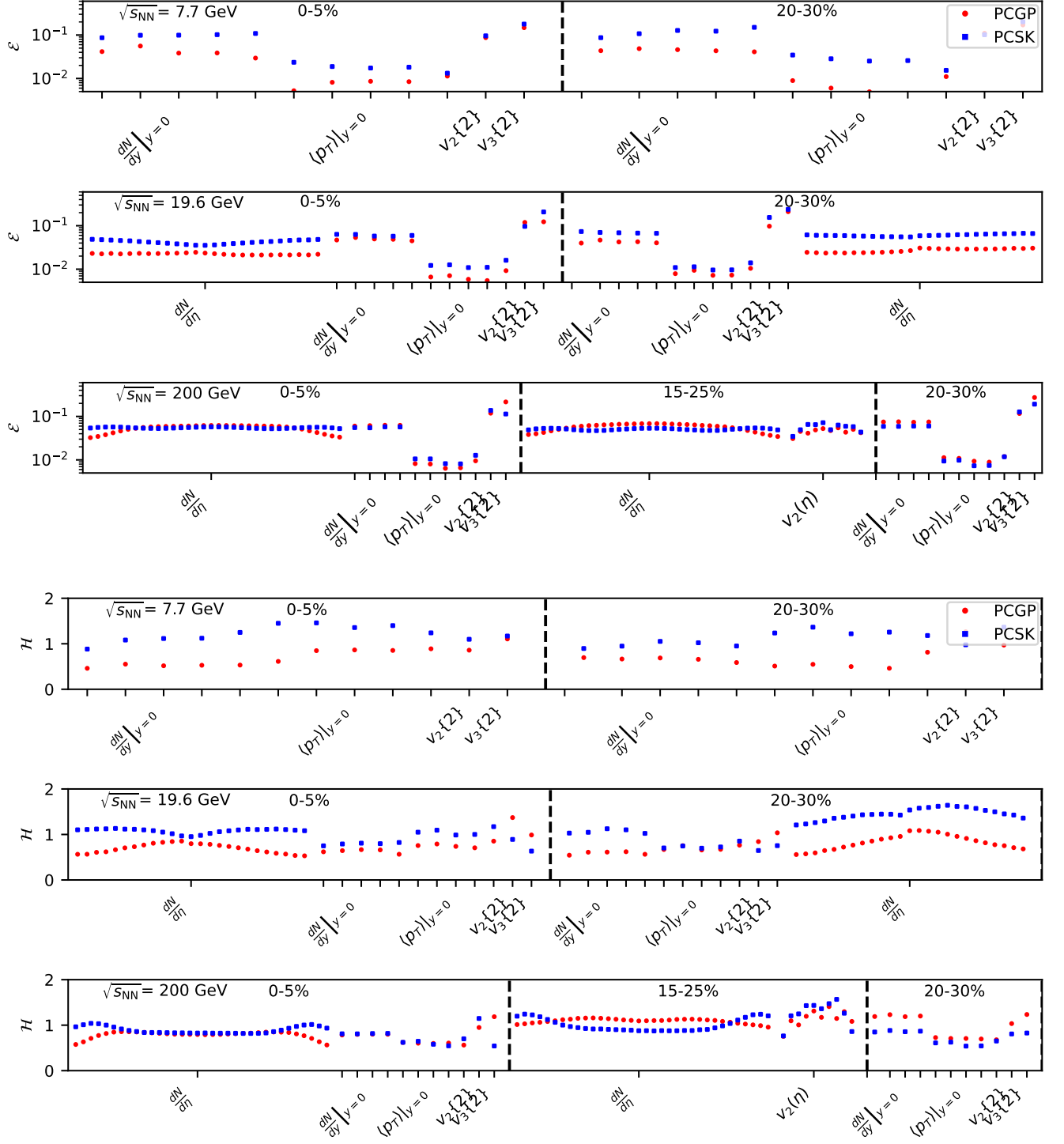


FIG. 3. The averaged root mean square error \mathcal{E} (top) and the uncertainty estimation metric \mathcal{H} bottom for both emulation strategies for all observables.

emulators as surrogates for the hybrid model [106, 107]. These emulators are trained on the simulation outputs corresponding to the sampled parameter sets, enabling efficient predictions of mean $\mu(\theta)$ and covariance $C(\theta)$

for the full parameter space.

The likelihood function in eq. (10) is approximated using the GP emulator as:

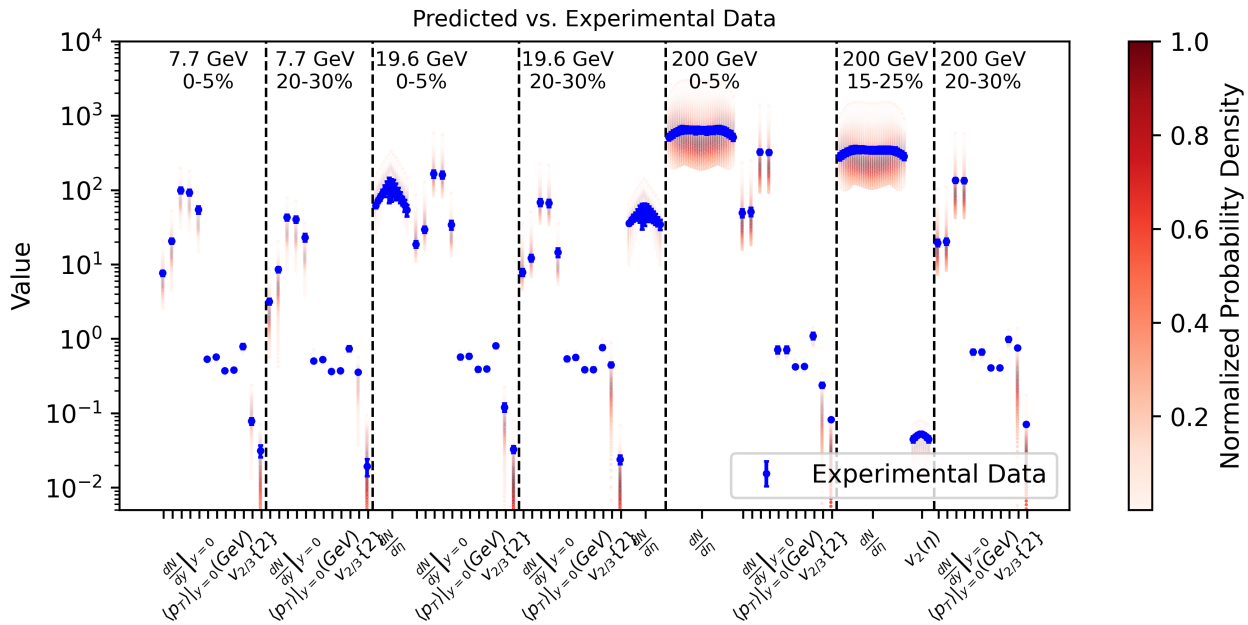


FIG. 4. Probability distribution of the posterior observables for the full prior range, compared to the experimental data points used in this study. For mean transverse momenta, the width of the distribution is comparable to the size of the data markers.

$$\mathcal{P}(\mathbf{y}_{\text{exp}}|\boldsymbol{\theta}) \approx \frac{1}{\sqrt{|2\pi\mathbf{V}(\boldsymbol{\theta})|}} \exp\left[-\frac{1}{2}(\boldsymbol{\mu}(\boldsymbol{\theta}) - \mathbf{y}_{\text{exp}})^{\top}\mathbf{V}(\boldsymbol{\theta})^{-1}(\boldsymbol{\mu}(\boldsymbol{\theta}) - \mathbf{y}_{\text{exp}})\right], \quad (11)$$

where $\mathbf{V}(\boldsymbol{\theta}) = \mathbf{C}(\boldsymbol{\theta}) + \boldsymbol{\Sigma}$. This approach significantly reduces computational costs while maintaining high accuracy.

For this work, we utilize the BAND framework, specifically the surmise library [108].

Using the trained GP emulators, we can obtain the posterior distribution of model parameters, $\mathcal{P}(\boldsymbol{\theta}|y_{\text{exp}})$, following Bayes' theorem by sampling the (in our case) uniform prior $\mathcal{P}(\boldsymbol{\theta})$ with the Monte Carlo Markov Chain (MCMC) method,

$$\mathcal{P}(\boldsymbol{\theta}|y_{\text{exp}}) \propto \mathcal{P}(y_{\text{exp}}|\boldsymbol{\theta})\mathcal{P}(\boldsymbol{\theta}). \quad (12)$$

Here $\mathcal{P}(y_{\text{exp}}|\boldsymbol{\theta})$ is the likelihood for the model results with parameter $\boldsymbol{\theta}$ to agree with the experimental data y_{exp} .

E. Posterior Estimation via MCMC

The posterior distribution is sampled using Markov Chain Monte Carlo (MCMC) methods, specifically the Preconditioned Monte Carlo (PMC) algorithm implemented in the pocoMC package [109, 110]. PMC integrates persistent sampling, normalizing flow preconditioning, and a gradient-free Markov kernel. The PMC algorithm incrementally adjusts an inverse temperature parameter, transitioning from the prior to the posterior

distribution. It enables effective exploration of complex posterior distributions without relying on gradient information. This approach is particularly advantageous for high-dimensional and computationally intensive models, as it enhances sampling efficiency and accuracy.

Normalizing flow preconditioning, a powerful technique based on neural networks, allows for efficient learning of complex high-dimensional distributions. It has been successfully applied in diverse contexts, including image processing [111] and matrix element integration [112]. The combination of these techniques ensures accurate exploration of the posterior distribution, even for high-dimensional and computationally intensive models.

The corresponding codebase of [74] was also used for generating the emulators and performing the posterior generation.

V. VALIDATION

Validation is a crucial process when performing a Bayesian analysis, as it ensures trustworthy results and spots potential issues in the parameter estimation.

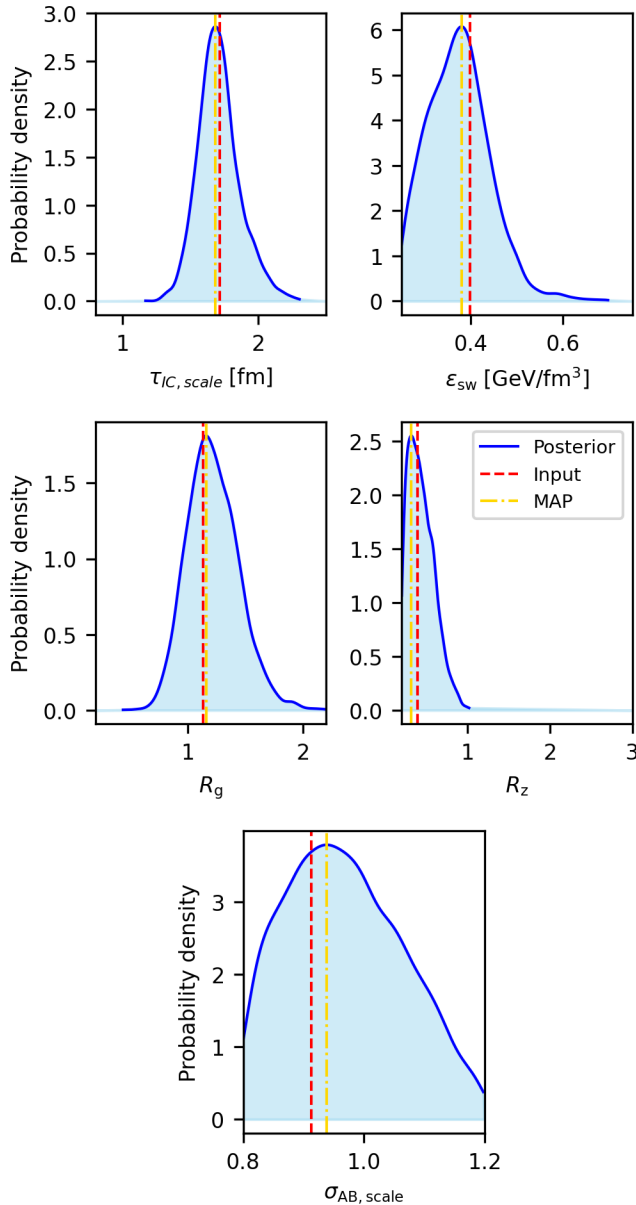


FIG. 5. Posterior of the technical parameters in the closure test. The red vertical line is the value of the parameter generating the pseudo-experimental data, the golden vertical line represents the maximum-a-posteriori value.

A. Emulator validation

We use the test metric for benchmarking proposed in [74] to choose the most accurate GP configuration in our setup. To quantify the prediction error of the GP emulators, one defines

$$\mathcal{E} \equiv \sqrt{\left\langle \left(\frac{\text{prediction} - \text{truth}}{\text{truth}} \right)^2 \right\rangle} \quad (13)$$

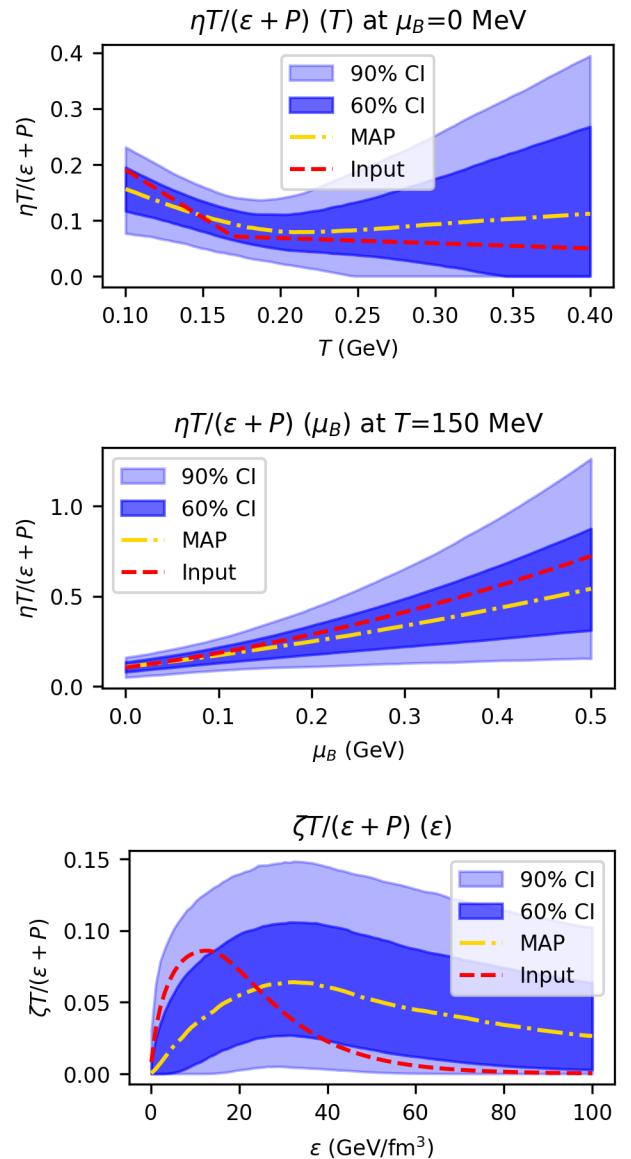


FIG. 6. Posterior of the viscosities in the closure test. From top to bottom: the shear viscosity as a function of temperature for vanishing baryochemical potential, the shear viscosity as a function of baryochemical potential at fixed temperature, and the bulk viscosity as a function of the energy density. The red line is the input parameterization, and the golden line represents the maximum-a-posteriori. The bands represent the 60% and 90% confidence interval of the posterior.

for each observable in the analysis, whereas the emulators uncertainty is quantified as

$$\mathcal{H} \equiv \ln \left(\sqrt{\left\langle \left(\frac{\text{prediction} - \text{truth}}{\text{prediction uncertainty}} \right)^2 \right\rangle} \right). \quad (14)$$

For an accurate prediction, we expect the values of $\mathcal{E} \rightarrow 0$ and $\mathcal{H} \rightarrow 0$. In the case where $\mathcal{H} > 0$, the emulator

gives uncertainties that are too small compared to the actual error away from the true values; when $\mathcal{H} < 0$, the returned uncertainty estimates are too conservative. To determine prediction and truth, 15 parameter sets were excluded from the training of the GP. Then, the prediction for the value and its uncertainty at the excluded parameter sets are compared to the simulation results at these values. The values of the benchmarking metric for each observable can be found in fig. 3, for two prescriptions of GP emulation which were found in [74] to perform well: PCGP (Principal Component Gaussian Process) and PCSK (Principal Component Stochastic Kriging). They both use the PCA-decomposition and the Matérn kernel. For each principal component $t_l(\boldsymbol{\theta}) = \mathbf{s}_l^T \tilde{\mathbf{y}}_{\text{sim}}(\boldsymbol{\theta})$, where $\tilde{\mathbf{y}}_{\text{sim}}$ is the standardized output, a GP model provides a predictive mean $m_l(\boldsymbol{\theta})$ and variance $s_l^2(\boldsymbol{\theta})$. In other words, each principle component is drawn from a Gaussian distribution with mean $m_l(\boldsymbol{\theta})$ and standard deviation $s_l^2(\boldsymbol{\theta})$, where $m_l(\boldsymbol{\theta}) = \mathbf{k}_l^T \mathbf{K}_l^{-1} \mathbf{t}_l$ and $s_l^2(\boldsymbol{\theta}) = k_l(\boldsymbol{\theta}, \boldsymbol{\theta}) - \mathbf{k}_l^T(\boldsymbol{\theta}) \mathbf{K}_l^{-1} \mathbf{k}_l(\boldsymbol{\theta})$. Here, $\mathbf{k}_l(\boldsymbol{\theta}) = [k_l(\boldsymbol{\theta}, \boldsymbol{\theta}_i^{\text{tr}})]_{i=1}^n$ denotes the covariance vector between n training parameters $\{\boldsymbol{\theta}_1^{\text{tr}}, \dots, \boldsymbol{\theta}_n^{\text{tr}}\}$ and any chosen parameter $\boldsymbol{\theta}$, and $\mathbf{K}_l = [k_l(\boldsymbol{\theta}_i^{\text{tr}}, \boldsymbol{\theta}_j^{\text{tr}}) + \delta_{i,j} r_{l,i}]_{i,j=1}^n$ represents the covariance matrix between the n training parameters. $r_{l,i}$ is the square of the statistical uncertainty of the l -th principal component at the training point i , and is only present for PCSK. As a result, only PCSK includes also the uncertainty of the model predictions in the emulation.

The top three panels of fig. 3 show \mathcal{E} , and the bottom three panels show \mathcal{H} . From top to bottom, the energy increases, whereas the centrality decreases from left to right, with centrality classes separated by a line. Each x-tick represents a different observable. We observe that for both prescriptions, errors remain within acceptable bounds. The biggest deviations occur for the integrated flow, probably due to the higher impact of fluctuations. In comparison to [74], we observe basically no rapidity dependence of the errors. Additionally, for the majority of data points, PCGP outperforms PCSK substantially. A similar picture emerges for the uncertainty metric. It is for most datapoints considerably closer to zero than for PCSK, and therefore underestimates the uncertainty less. This is remarkable as PCSK takes the standard deviation of the training data into account, whereas PCGP does not. However, such behavior can be also observed for several observables in [74]. It is currently not clear why PCSK provides less conservative estimates for the uncertainty, although it includes the uncertainty from the model. This question is left for further studies. In the meantime, we note that PCSK is not suited for giving a good uncertainty estimation. Of the proposed preprocessing methods, namely logscaling the observables and performing a PCA the viscosity parameterizations, none could improve the performance in these metrics. Therefore, they were not employed. As PCGP outperforms PCSK in most metrics, we continue using this approach for the rest of this work.

B. Prior validation

A further validation is the consideration if the prior range chosen is sufficient to fit experimental data. Figure 4 shows the probability distribution for values of the observables to be fitted to experimental data. In simple words, it shows the likelihood for each observable to be predicted if a random point were to be chosen from prior space. We see that the experimental data points lie all within the this range. However, we see that certain experimental datapoints lie closer to the edges of the range, especially flows at higher collision energies and $\frac{dN}{d\eta}$ at 19.6 GeV. It is important to note however that this alone does not guarantee that experimental data can be precisely fitted, as not necessarily all data points can be fitted correctly simultaneously.

C. Closure test

As a next step, we perform a closure test. Closure tests are crucial in validating that model parameters can be successfully constrained. They can, for example, detect if the number of points in prior space is too low, if data is insensitive to a parameter or if there are degeneracies in a model, allowing disjunct regions of the parameter space to result in the same predictions. Conducting a closure test follows a similar idea than the emulator validation before. Again, one of the training points is separated out. However, this time the predictions of this training point are considered as pseudo-experimental data. Now, the whole toolchain, starting from the Gaussian process emulation and continuing to the construction of the posterior using MCMC, is performed under the assumption of this pseudo-experimental data. In an ideal case, the original input parameters are reproduced, and the peaks of the posterior are close to these values. If the data is sufficient to constrain a parameter well, one expects strongly pronounced peaks. Figure 5 shows the posterior distributions of the technical parameters. Especially the scaling factor for the fluidization time and the smearing parameters are well constrained. The distribution is wider for the particlization energy density and especially for the late stage rescattering cross section scaling. Indeed, although for the latter, the MAP estimate agrees quite well with the original parameter, the distribution is very wide, showing only weak constraints.

Continuing to the viscosities in fig. 6, we see good constraints for the shear viscosity. Both as a function of temperature and as a function of baryochemical potential, the original parameterization lies comfortably in the 60% confidence interval. This means that the Bayesian inference could extract the correct functional dependence. For the bulk viscosity, this holds in general, too. However, the quality of the posterior is here decreased and the original parameterization lies at the boundaries between the more strict 60% confidence interval and the 90% confidence interval. This is however still in the statistically

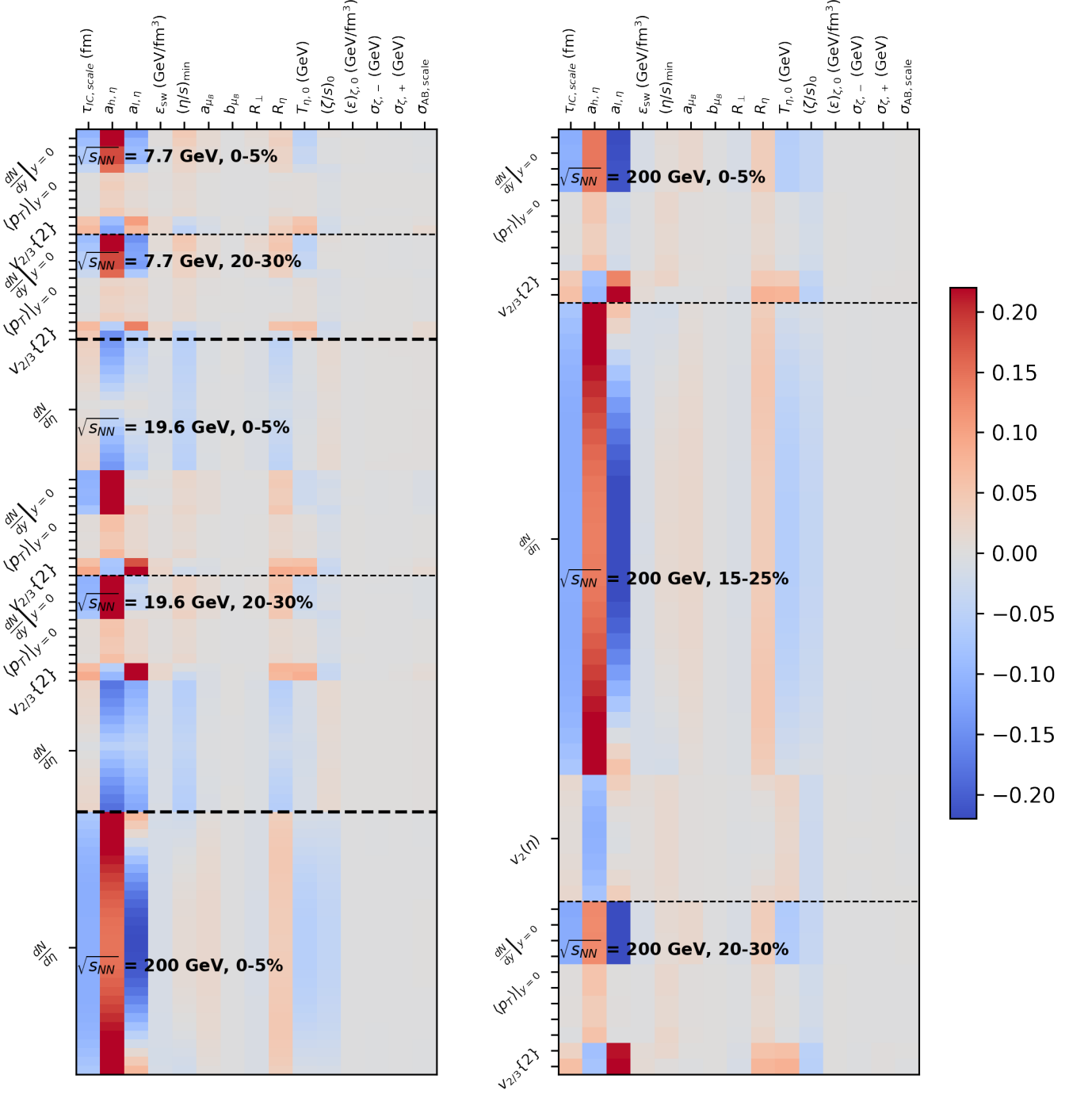


FIG. 7. Normalized partial derivatives of observables with respect to parameters of the simulation (response matrix) averaged over multiple prior points. Positive values (red) mark an increase in the observable with the value of the parameter, negative values (blue) mark a decrease.

acceptable range.

With this successful validation of our approach, we can now move on to the results on applying this setup to experimental data.

VI. RESULTS

We want to present now results obtained with our model.

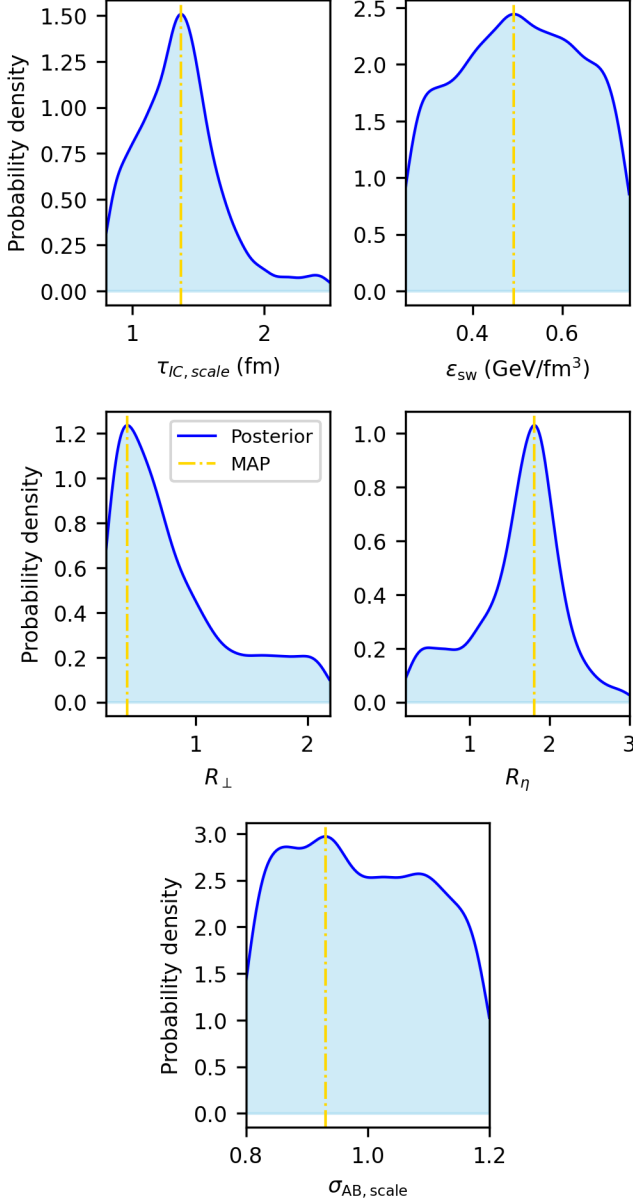


FIG. 8. Posterior of the technical parameters. The golden vertical line represents the maximum-a-posteriori value.

A. Sensitivity Analysis

In a first step, we want to gain an understanding of how the different parameters affect observables. An easy accessible tool to do so is the response matrix, which looks at partial derivatives of observables with respect to the model parameters using the centered finite difference method. There are two important points to note about this: On the one hand, this is independent of the posterior, as this can be performed on the emulated prior directly. However, we perform this analysis in the center of the posterior. On the other hand, the response matrix

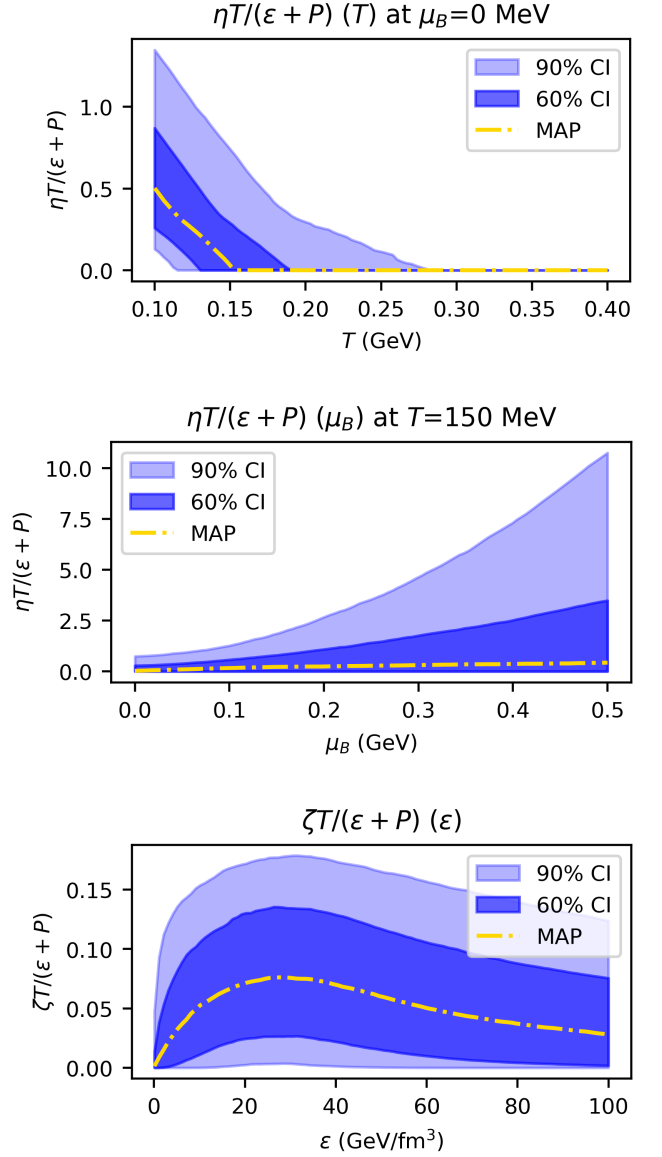


FIG. 9. Posterior of the viscosities. From top to bottom: the shear viscosity as a function of temperature for vanishing baryochemical potential, the shear viscosity as a function of baryochemical potential at fixed temperature, and the bulk viscosity as a function of the energy density. The golden line represents the maximum-a-posteriori. The bands represent the 60% and 90% confidence interval of the posterior.

is a local, linearized statement, and can change throughout the prior space, as there is potentially interaction between the parameters. Such relationships are contained in more evolved descriptions like Sobol indices. To gain a first overview, we take a look at a normalized, averaged response matrix which aggregates the contributions of many prior points. The results are displayed in fig. 7. Positive (red) areas mean that a positive correlation between observable and parameter, negative (blue) means

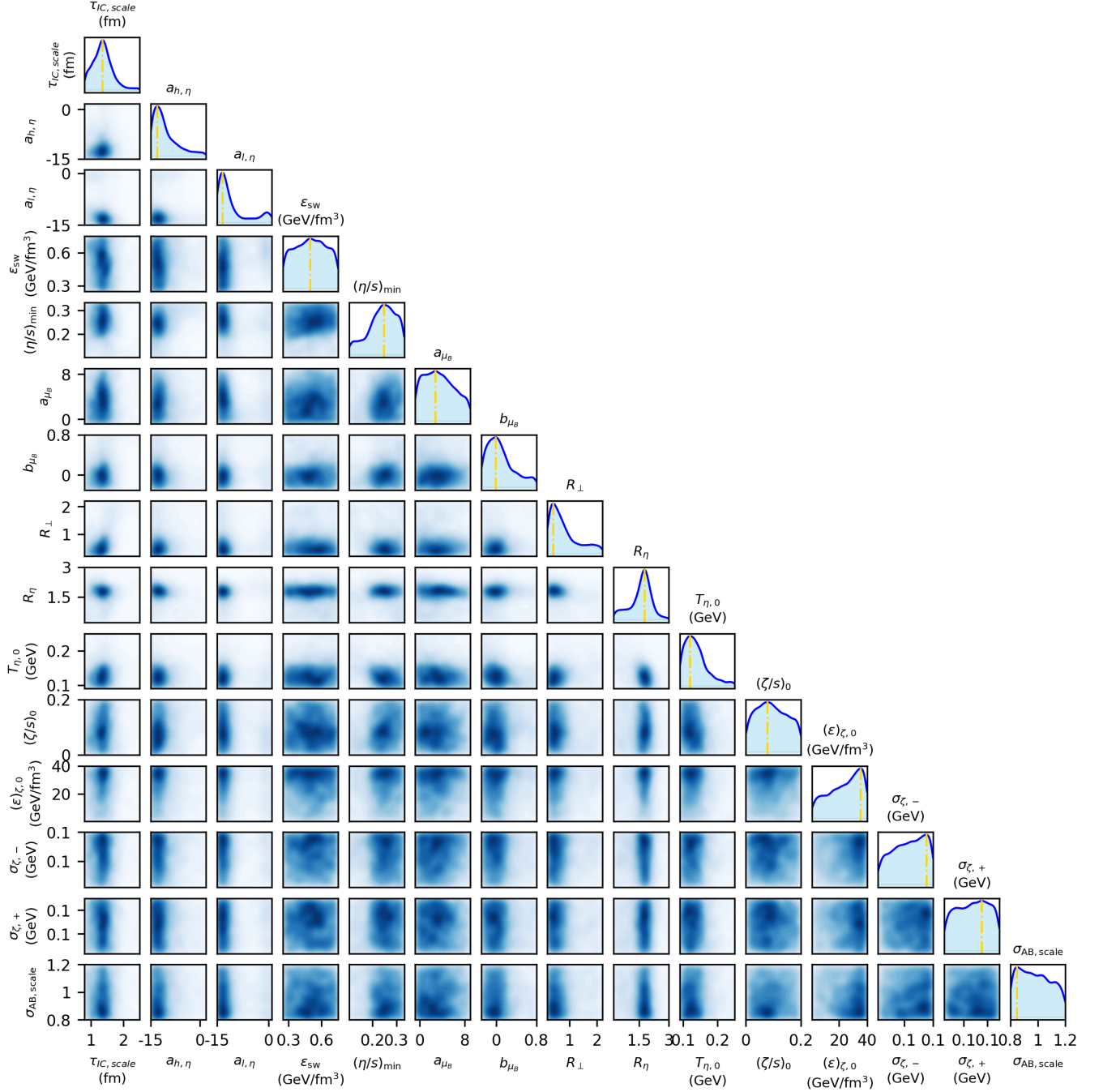


FIG. 10. Full posterior for all parameters. The diagonal shows the distribution for each parameter, whereas the off-diagonal shows the probability distribution for a combination of two parameters.

a negative correlation, i.e. a decrease in the parameter means an increase in the observable. We want to point out some striking observations.

The fluidization time scale $\tau_{IC, scale}$ shows a high sensitivity in many observables. Most notably the flows, but also multiplicities. Whereas at midrapidity, one can observe consistently a negative correlation, at higher rapidities at intermediate energies, the fluidization time

is positively correlated with multiplicities. This shows the complex effect of performing initial scatterings for a longer time. A possible explanation for this are differences in the treatment of particles in SMASH at higher and lower collision energies - at high energies, the particles remain generally unformed after the first collision, and cannot interact again, whereas secondary collisions are more likely at lower collision energies. We also note

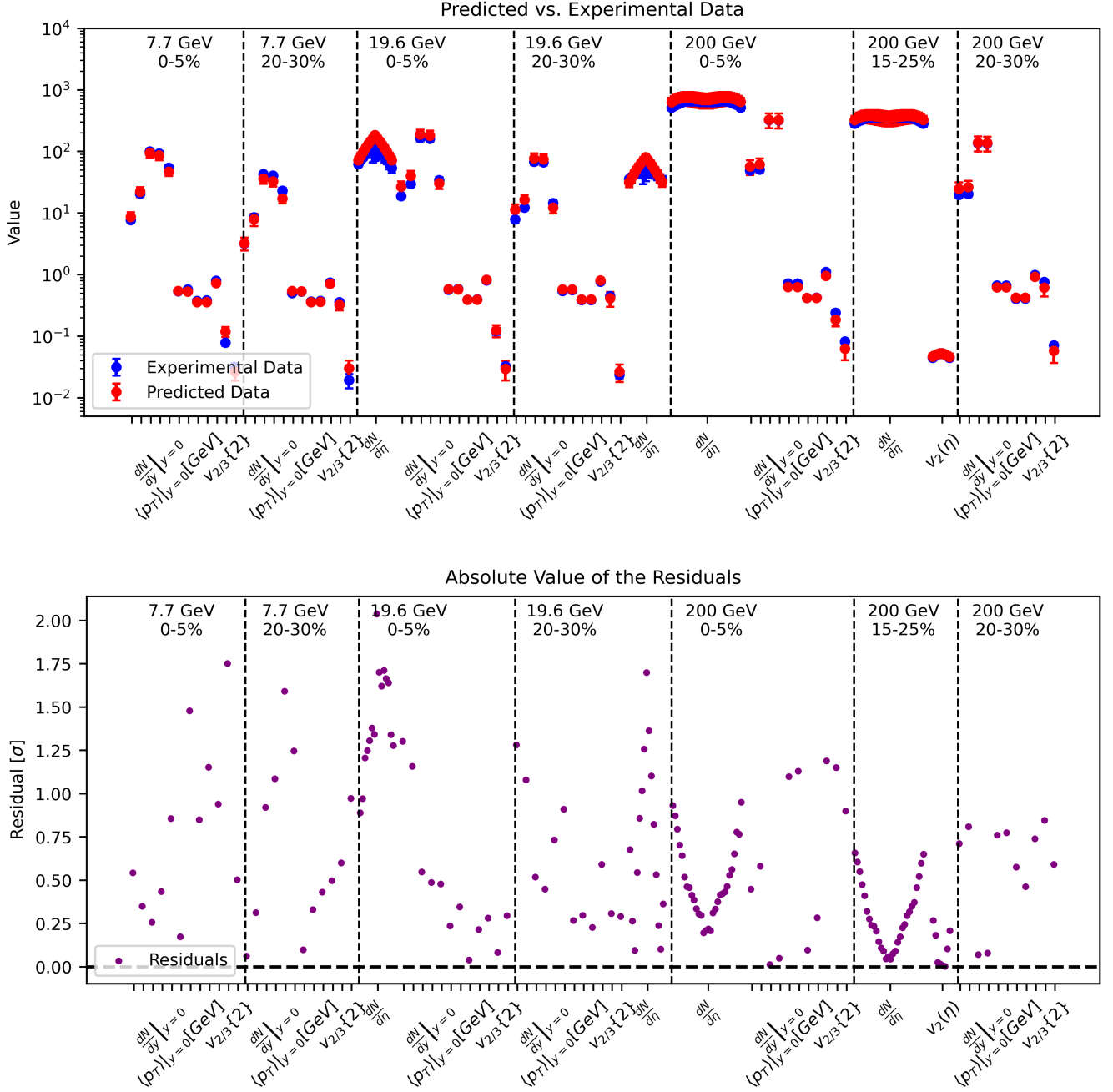


FIG. 11. Comparison of predictions of observables from the posterior with experimental values (top). Residuals between predictions and experimental data in multiples of standard deviations (bottom).

the positive correlation between flows and fluidization time scale; this is contradictory to earlier observed behaviour [35]. It suggests that early transport is more efficient in generating momentum anisotropy than the hydrodynamic stage, which could be an effect of the presence of substantial values of the transport coefficients. The longitudinal smearing increases multiplicities at high energies while decreasing it in the high rapidity regions at intermediate energies. This gives a more nuanced picture

on their effect for the multiplicities with respect to [35]. Another important parameter is the kink temperature of the shear viscosity, $T_{\eta,0}$. It shows in general a similar behaviour to the fluidization time scaling, although it decreases multiplicities in the full rapidity spectrum at intermediate energies. The steepnesses of the linear temperature dependence of the shear viscosity show strong impacts on a wide range of observables, with a substantial presence of rapidity dependence. Note that the correla-

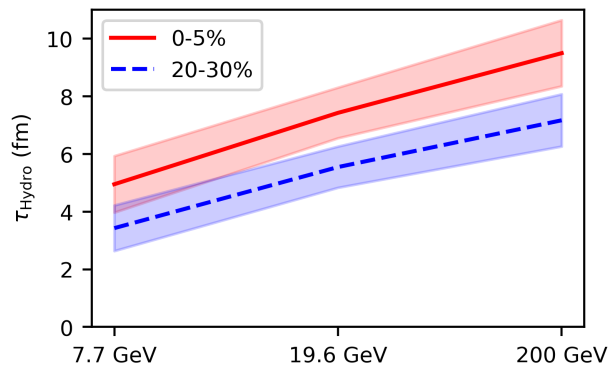


FIG. 12. MAP of the duration of the hydrodynamic evolution in the posterior.

tions are of opposite sign due to the additional minus sign for low temperatures in eq. (5). In general, the expected behavior is realised that increasing the shear viscosity decreases anisotropic flows. There is only weak dependency on parameters related to baryochemical potential. For bulk viscosity, only the parameter of its magnitude is relevant. All other viscous parameters do not affect the observables strongly. The same can be said about the rescattering cross section scaling and the density dependence of the shear viscosity, which show relatively small signals. Therefore, we can expect weaker constraints on these parameters.

B. Posterior Predictions

In a first step, we take a look at the posterior distribution of technical parameters again, which can be found in fig. 8. We observe a preference for slightly increased fluidization time, which contrasts with the results of [62] preferring a minimal fluidization time. However, both this and the earlier study find a particlization energy density around $0.5 \frac{\text{GeV}}{\text{fm}^3}$ to be optimal, albeit at substantial uncertainty. The preferred smearing parameters differ substantially between both studies. The current model prefers minimal smearing in the transverse plane and substantial smearing in the longitudinal direction. Regarding the scaling of cross sections in the late stage rescattering, the uncertainty is high and therefore the result is statistically consistent with 1.

Looking at viscosities in fig. 9, the observations drawn earlier from the seen for the sensitivity analysis become apparent again: the constraints on both the bulk viscosity and the baryochemical potential dependence are too weak to efficiently constrain these values and a wide range of values is consistent with the data.

The situation is different for the temperature dependence, where a rapidly decreasing shear viscosity is preferred, which stays at zero from around 150 - 250 MeV on. The origin of this becomes more clear looking at the

full posterior of all parameters in fig. 10. We can see that, although there is a kink with $(\eta/s)_{\text{min}} \neq 0$, the steepness on both sides is nearly identical, leading to the cutoff to negative values setting the shear viscosity to 0 for high temperatures. Interestingly, this is a degenerated form - after all, a kink with $(\eta/s)_{\text{min}} = 0$ and any negative steepness for higher temperatures could reach such a configuration. It is currently not clear why such a setup was preferred. Nevertheless, it seems that our model strongly prefers vanishing shear viscosities in the QGP phase, but substantial viscosities near particlization. All maximum-a-posteriori values can be also found in table V.

There are further insights to be gained from fig. 10. We see that b_{μ_B} is strongly peaked at 0. Therefore, much of the uncertainty for baryochemical potential dependence comes from a_{μ_B} , which is insufficiently constrained. Furthermore, we see only very limited interactions between the parameters, which can be most easily identified by diagonal structures in the triangle plot. A trace of this can be seen for $\tau_{\text{IC, scale}}$ and R_{\perp} .

We want to point out that our tune reproduces experimental data at a very high quality. In fig. 11, we show a comparison between the experimental data and the predicted values from the model. For all data points, the difference is around 2 standard deviations or lower. It is interesting to note that with regards to the longitudinal properties, at high energies, our model describes midrapidity multiplicities better than data at forward or backward rapidities, whereas at intermediate energies, this is inverted. This points to a general limitation of this model to fully capture longitudinal dynamics as a function of collision energies. The comparison of the MAP observable predictions with experimental measurements is also provided in a linear scale and split by observables in the appendix in fig. 18, fig. 19 and fig. 20.

C. Hydrodynamic evolution time

Both $\tau_{\text{IC, scale}}$ and ϵ_{switch} encode the duration of the hydrodynamic evolution, as they determine the starting and ending point, respectively. This motivates the study of τ_{Hydro} , the time which is spent in the hydrodynamic evolution. This time is also very crucial for the fit as it is this time frame of the evolution where viscosities can be tuned for modifying the viscosity. Figure 12 shows the maximum a posteriori for the duration of the hydrodynamic evolution for different systems. As expected, it increases both with collision energy and centrality. The values roughly agree with the ones reported for the default setup in [12].

This is no coincidence as τ_{Hydro} has a strong effect on observables. Figure 13 shows the correlation between observables and the hydrodynamic evolution time. Especially for yields and for flows at low energies, the correlation is significant. The reason for the flows being affected stronger at low energies can be attributed to the

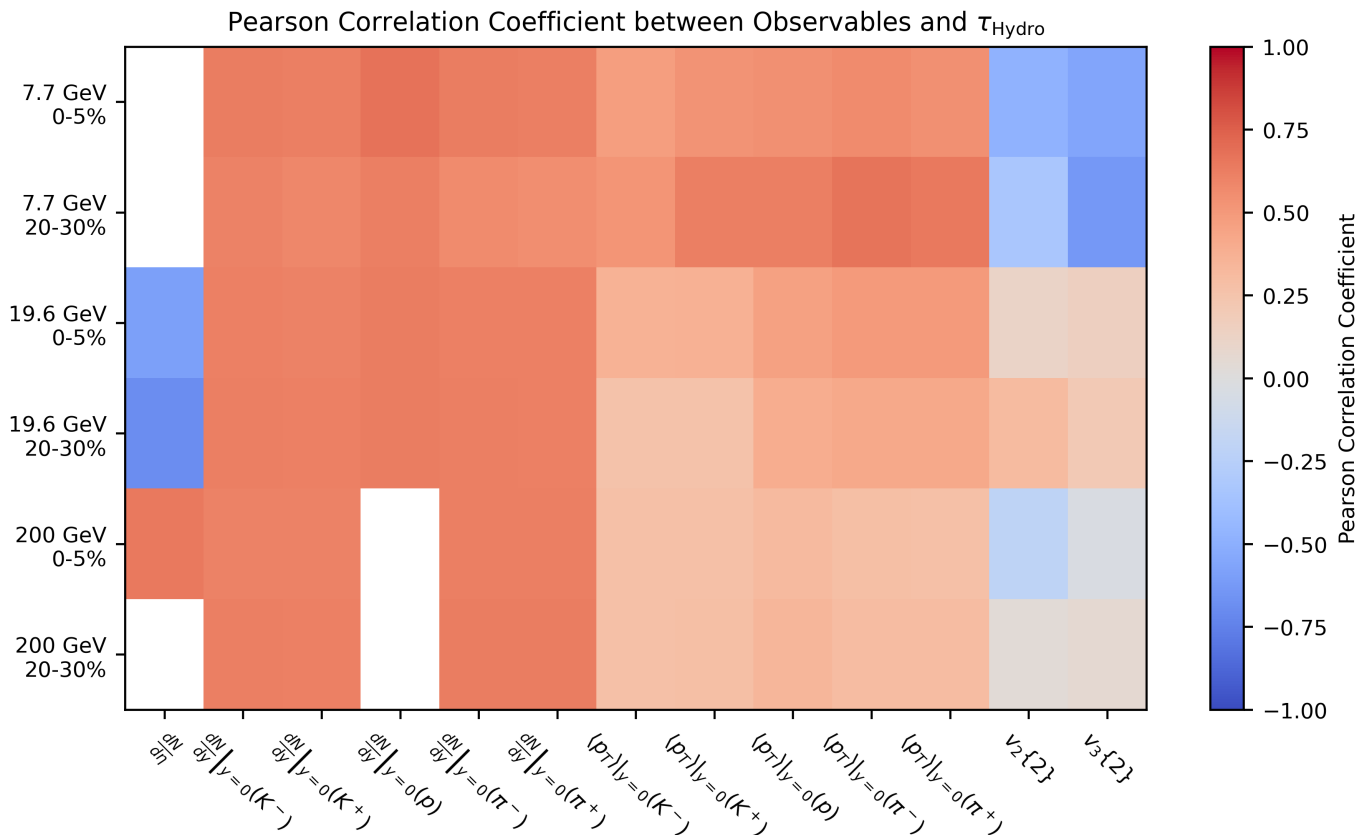


FIG. 13. Pearson correlation coefficient between the hydrodynamic evolution duration and observables used to train the fit. White squares signify observables where were not used at the respective energies/centralities. For spectra, the average over the data points is displayed.

medium of lower temperature and higher baryochemical potential, which yields higher viscosities.

Nevertheless, τ_{Hydro} can not be seen as a parameter of the system, replacing $\tau_{\text{IC, scale}}$ and ϵ_{switch} . Increasing both of these parameters to yield a similar average τ_{Hydro} would not amount to the same observables, as the evolution of the system in the early and late stages is fundamentally different. In other words, the hydrodynamic evolution can not be shifted throughout the evolution of the heavy ion collision. This can be seen also from the data directly: fig. 10 shows no diagonal structures between $\tau_{\text{IC, scale}}$ and ϵ_{switch} . Therefore, there are no corresponding pairs between these parameters leading to similar results.

D. Impact of data selection

We want to take a deeper look on the role of longitudinal data and the collision energies investigated. In a first step, we exclude data at $\sqrt{s_{\text{NN}}} = 200$ GeV. Figure 14 shows the effect on the technical parameters. While there is only a small change for the cross section scaling and

the transverse smearing, we observe substantial changes for other technical parameters. The initial stage scaling is now centered around 1. Most notably, however, is the strong preference for increased lifetime of the hydrodynamic stage and a strong reduction in longitudinal smearing. This strong change of parameters was most likely pushed by the residuals in multiplicity, which in the full fit were still substantial at intermediate energies, due to balancing out with the residuals at high rapidity data from high energies. Investigating further the viscosities, fig. 15 shows that data at high energies gives further constraints. Although the shear viscosity as a function of baryochemical potential is stronger constrained, this is a combination of two contributions: on the one hand, the additional rapidity-dependent data at 200 GeV contributes to the constraints. On the other hand, the additional data also constraints the temperature dependence, leading to a more constraint viscosity at $T = 150$ MeV at vanishing baryochemical potential. As this is scaled in proportion to the baryochemical potential, a more peaked temperature dependence also gives a less wide distribution as a function of μ_B .

The crucial role played by the longitudinal data is fur-

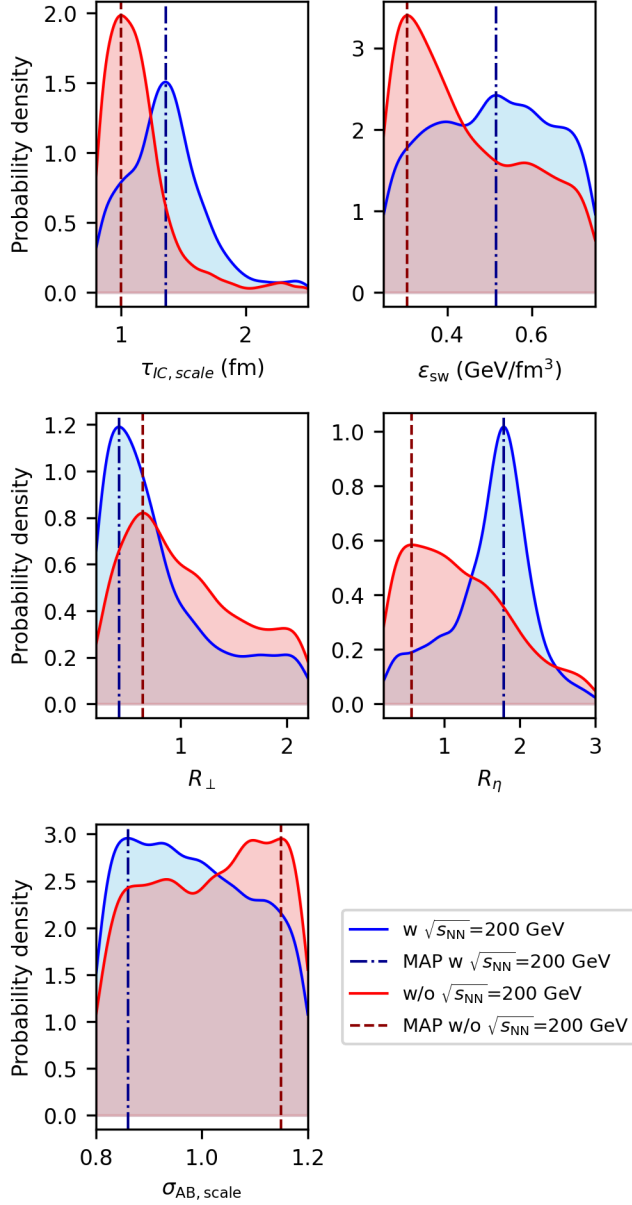


FIG. 14. Posterior of the technical parameters when including and excluding data at $\sqrt{s_{NN}} = 200$ GeV.

ther investigated in fig. 16 and fig. 17. Here, we compare the full dataset, but increase and reduce the rapidity cut. Regarding the technical parameters, cutting more strictly does not statistically significantly change most parameters, except increasing slightly the transversal smearing. For the relaxed cut, on the other hand, we see multiple of the technical parameters running into the boundaries of the prior ranges. We can therefore conclude that with our setup, we can not appropriately describe data at such high rapidities.

Regarding viscosities, we see that including high rapidity data gives additional constraints on the baryochem-

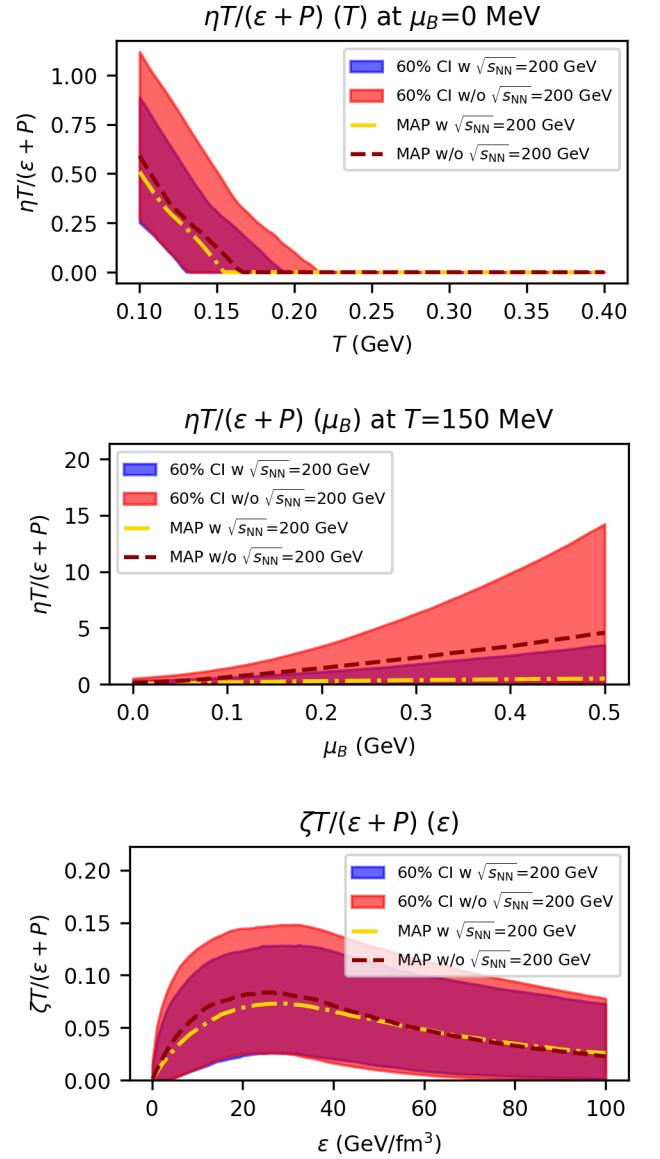


FIG. 15. Posterior of the viscosities when including and excluding data at $\sqrt{s_{NN}} = 200$ GeV. From top to bottom: the shear viscosity as a function of temperature for vanishing baryochemical potential, the shear viscosity as a function of baryochemical potential at fixed temperature, and the bulk viscosity as a function of the energy density. The bands represent the 60% confidence interval of the posterior.

ical potential dependence. However, it increases uncertainties of the bulk viscosity.

VII. CONCLUSIONS AND OUTLOOK

In this work, we have performed a Bayesian analysis of the (3+1)D SMASH-vHLE-hybrid model across a range of collision energies from 7.7 to 200 GeV. By com-

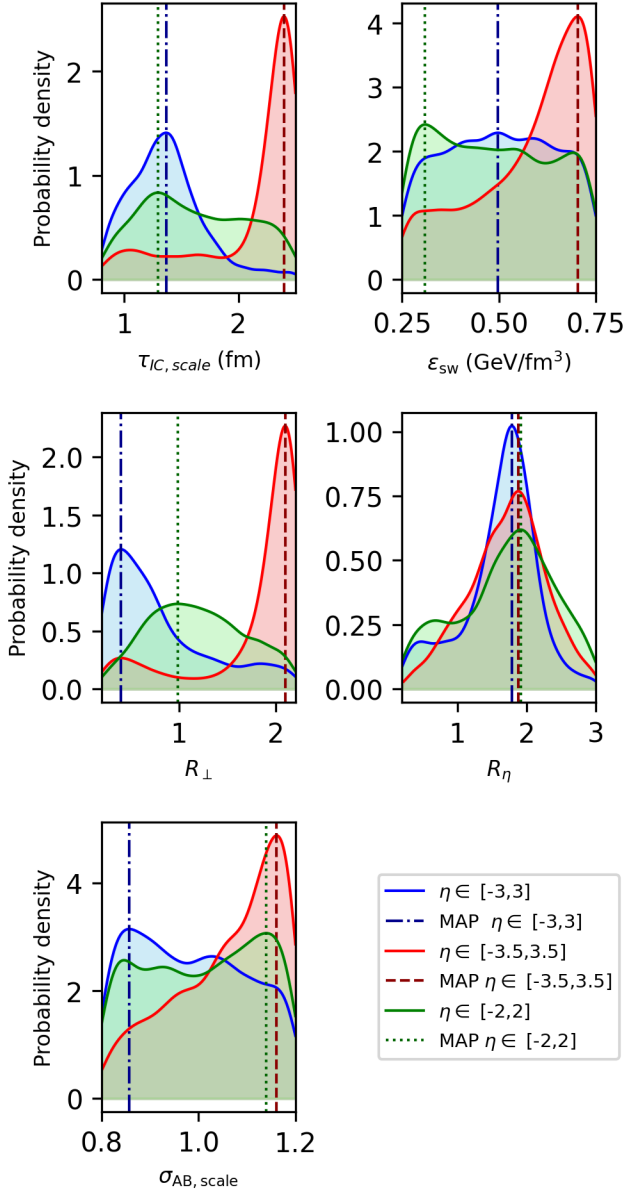


FIG. 16. Posterior of the technical parameters depending on the rapidity cut.

paring various sets of observables to a broad parameter space, we have constrained both the technical parameters (initialization time, transverse/longitudinal smearing, and switching energy density) and the temperature- and baryochemical-potential-dependent viscosities of the QGP. We have shown that, with the data currently available, the model strongly favors a near-zero shear viscosity in the high-temperature phase while permitting moderate-to-large values in the vicinity of the pseudo-critical region. Moreover, a wide range of bulk viscosity values remain compatible with the data, and the preferred baryochemical potential dependence is essentially consistent with no dependence at all, emphasizing the

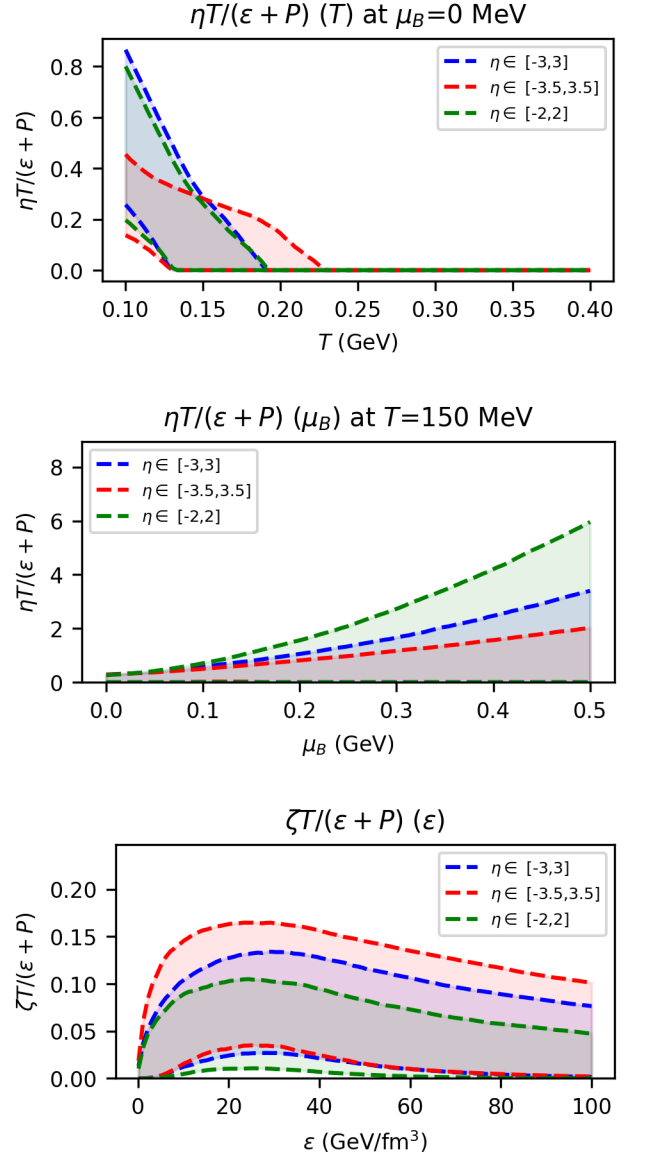


FIG. 17. Posterior of the viscosities depending on the rapidity cut. From top to bottom: the shear viscosity as a function of temperature for vanishing baryochemical potential, the shear viscosity as a function of baryochemical potential at fixed temperature, and the bulk viscosity as a function of the energy density. The bands represent the 60% confidence interval of the posterior.

limitation in present data precision.

These findings, especially regarding the nearly vanishing specific shear viscosity at higher temperatures, are at odds with several existing Bayesian analyses [63, 65, 67], which generally support a non-zero minimal shear viscosity in the QGP phase. We attribute our discrepancy partly to the reduced freedom in the initial state provided by the hadronic transport model, which lowers the degrees of freedom for tuning geometric fluc-

tuations and thus pushes certain parameters, such as the hydrodynamic onset time, into especially sensitive roles. While our analysis accommodates key beam energies and rapidity-dependent observables, even higher-statistics data would be needed for more definitive conclusions. A natural next step is to simplify the modelling assumptions by removing the presently unconstrained baryochemical potential dependence in order to reduce the dimensionality of the parameter space and isolate the most dominant effects. Similarly, it is a worthwhile study to investigate how much of the strong constraints on the high temperature shear viscosity can be attributed to the presence of bulk viscosity. We also envision direct comparisons to other initial-state scenarios, such as TRENTO, UrQMD, or McDIPPER, to examine the interplay between initial conditions and viscosity extractions. Ultimately, our investigation highlights the continued need for detailed experiments and improved multi-stage modeling to achieve a more robust picture of the QGP's transport properties over a wide range of beam energies.

Raw data of figures can be downloaded from the supplemental material [113].

ACKNOWLEDGMENTS

This work was supported by the Deutsche Forschungsgemeinschaft (DFG, German Research Foundation) – Project number 315477589 – TRR 211. N.G. acknowledges support by the Stiftung Polytechnische Gesellschaft Frankfurt am Main as well as the Studienstiftung des Deutschen Volkes. I.K. acknowledges support by the Czech Science Foundation under project No. 25-16877S. Computational resources have been provided by the GreenCube at GSI. N.G. wants to thank Hendrik Roch for the continued discussion and advise throughout this work.

Appendix A: MAP of parameters

The following table shows the maximum-a-posteriori of the parameters, equivalent to the golden lines in fig. 10, with $1-\sigma$ -confidence interval.

Appendix B: MAP observable predictions

In the following, we show the maximum a posterior observable predictions in comparison to experimental data. References for the experimental data can be found in table IV.

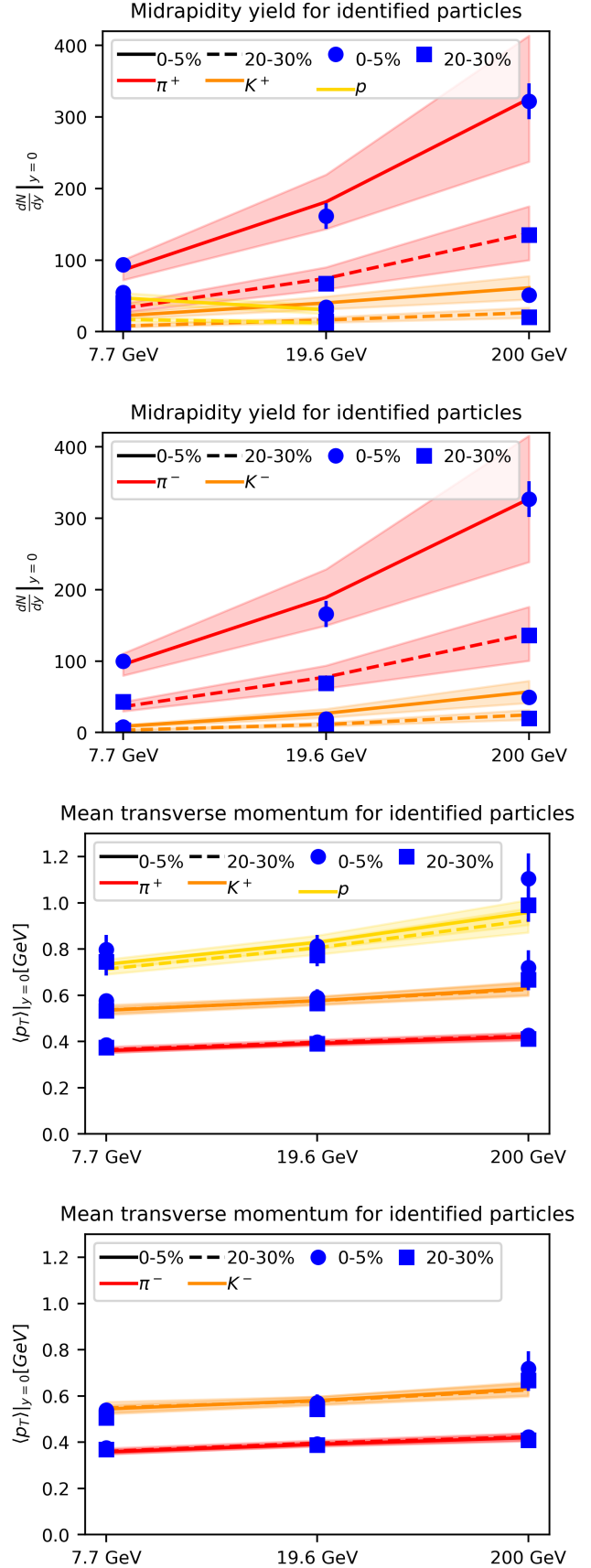


FIG. 18. Comparison of predictions of observables from the posterior with experimental values for bulk observables.

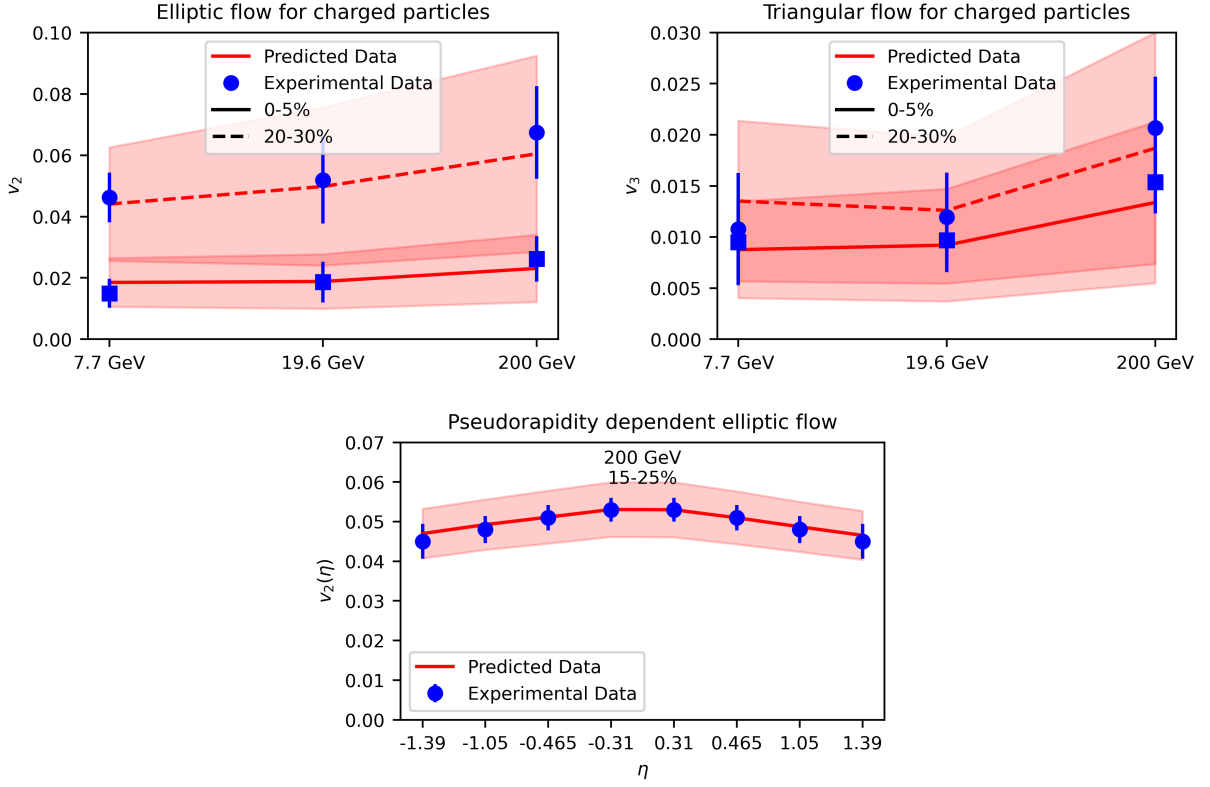


FIG. 19. Comparison of predictions of observables from the posterior with experimental values for flow data.

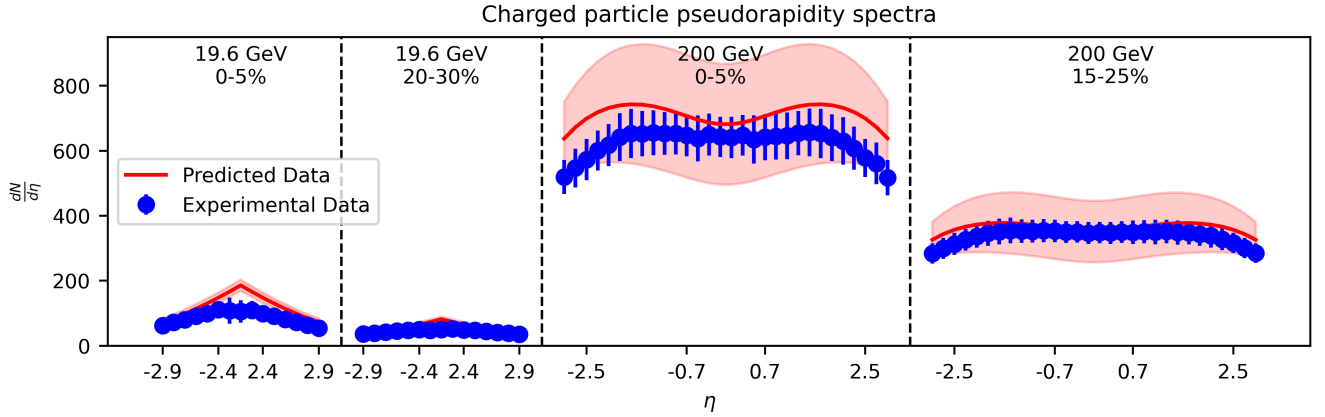


FIG. 20. Comparison of predictions of observables from the posterior with experimental values for pseudorapidity yield.

Parameter	MAP	
R_{\perp}	$0.6321^{+0.7465}_{-0.3018}$	fm
R_{η}	$1.6955^{+0.3611}_{-0.6767}$	fm
$\tau_{IC,scale}$	$1.3405^{+0.2889}_{-0.3019}$	
ϵ_{switch}	$0.5029^{+0.1612}_{-0.1668}$	$\frac{\text{GeV}}{\text{fm}^3}$
$a_{l,\eta}$	$-12.5323^{+7.8258}_{-1.6009}$	
$a_{h,\eta}$	$-11.7024^{+4.6039}_{-2.2125}$	
T_0	$0.1313^{+0.0395}_{-0.0267}$	GeV
$(\eta/s)_{\min}$	$0.2185^{+0.0832}_{-0.0994}$	
a_{μ_B}	$3.2318^{+3.3766}_{-2.7164}$	
b_{μ_B}	$0.0373^{+0.3290}_{-0.2110}$	
ζ_0	$0.0916^{+0.0675}_{-0.0582}$	
ϵ_{ζ}	$25.7295^{+10.2582}_{-15.2152}$	$\frac{\text{GeV}}{\text{fm}^3}$
$\sigma_{\zeta,-}$	$0.0589^{+0.0289}_{-0.0344}$	
$\sigma_{\zeta,+}$	$0.0824^{+0.0457}_{-0.0480}$	
$\sigma_{AB,scale}$	$0.9769^{+0.1451}_{-0.1240}$	

TABLE V. MAP of all parameters of the model.

- [1] P. Achenbach *et al.*, Nucl. Phys. A **1047**, 122874 (2024), arXiv:2303.02579 [hep-ph].
- [2] M. Arslanok *et al.*, (2023), arXiv:2303.17254 [nucl-ex].
- [3] H. Caines (STAR), in *44th Rencontres de Moriond on QCD and High Energy Interactions* (2009) pp. 375–378, arXiv:0906.0305 [nucl-ex].
- [4] B. Mohanty (STAR), J. Phys. G **38**, 124023 (2011), arXiv:1106.5902 [nucl-ex].
- [5] J. T. Mitchell (PHENIX), Nucl. Phys. A **904-905**, 903c (2013), arXiv:1211.6139 [nucl-ex].
- [6] G. Odyniec, EPJ Web Conf. **95**, 03027 (2015).
- [7] M. M. Aggarwal *et al.* (STAR), (2010), arXiv:1007.2613 [nucl-ex].
- [8] X. Luo and N. Xu, Nucl. Sci. Tech. **28**, 112 (2017), arXiv:1701.02105 [nucl-ex].
- [9] A. Bzdak, S. Esumi, V. Koch, J. Liao, M. Stephanov, and N. Xu, Phys. Rept. **853**, 1 (2020), arXiv:1906.00936 [nucl-th].
- [10] X. An *et al.*, Nucl. Phys. A **1017**, 122343 (2022), arXiv:2108.13867 [nucl-th].
- [11] X.-Y. Wu, G.-Y. Qin, L.-G. Pang, and X.-N. Wang, Phys. Rev. C **105**, 034909 (2022).
- [12] A. Schäfer, I. Karpenko, X.-Y. Wu, J. Hammelmann, and H. Elfner (SMASH), Eur. Phys. J. A **58**, 230 (2022), arXiv:2112.08724 [hep-ph].
- [13] A. Nandi, L. Kumar, and N. Sharma, Phys. Rev. C **102**, 024902 (2020).
- [14] B. Schenke, C. Shen, and P. Tribedy, Phys. Rev. C **102**, 044905 (2020), arXiv:2005.14682 [nucl-th].
- [15] L. Du and U. Heinz, Comput. Phys. Commun. **251**, 107090 (2020).
- [16] G. Nijs, W. van der Schee, U. Gürsoy, and R. Snellings, Phys. Rev. C **103**, 054909 (2021), arXiv:2010.15134 [nucl-th].
- [17] J. H. Putschke *et al.*, (2019), arXiv:1903.07706 [nucl-th].
- [18] L.-G. Pang, H. Petersen, and X.-N. Wang, Phys. Rev. C **97**, 064918 (2018), arXiv:1802.04449 [nucl-th].
- [19] Y. Akamatsu, M. Asakawa, T. Hirano, M. Kitazawa, K. Morita, K. Murase, Y. Nara, C. Nonaka, and A. Ohnishi, Phys. Rev. C **98**, 024909 (2018).
- [20] C. Shen, G. Denicol, C. Gale, S. Jeon, A. Monnai, and B. Schenke, Nucl. Phys. A **967**, 796 (2017).
- [21] I. A. Karpenko, P. Huovinen, H. Petersen, and M. Bleicher, Phys. Rev. C **91**, 064901 (2015).
- [22] C. Shen, Z. Qiu, H. Song, J. Bernhard, S. Bass, and U. Heinz, Comput. Phys. Commun. **199**, 61 (2016), arXiv:1409.8164 [nucl-th].
- [23] H. Petersen, J. Steinheimer, G. Burau, M. Bleicher, and H. Stöcker, Phys. Rev. C **78**, 044901 (2008).
- [24] H. Song, S. A. Bass, U. Heinz, T. Hirano, and C. Shen, Phys. Rev. Lett. **106**, 192301 (2011), [Erratum: Phys.Rev.Lett. 109, 139904 (2012)], arXiv:1011.2783 [nucl-th].
- [25] B. Schenke, S. Jeon, and C. Gale, Phys. Rev. Lett. **106**, 042301 (2011), arXiv:1009.3244 [hep-ph].
- [26] Z. Qiu, C. Shen, and U. Heinz, Phys. Lett. B **707**, 151 (2012), arXiv:1110.3033 [nucl-th].
- [27] C. Gale, S. Jeon, and B. Schenke, Int. J. Mod. Phys. A **28**, 1340011 (2013), arXiv:1301.5893 [nucl-th].
- [28] U. Heinz and R. Snellings, Ann. Rev. Nucl. Part. Sci. **63**, 123 (2013), arXiv:1301.2826 [nucl-th].
- [29] C. Shen and L. Yan, Nucl. Sci. Tech. **31**, 122 (2020), arXiv:2010.12377 [nucl-th].
- [30] G. D. Moore, in *Criticality in QCD and the Hadron Resonance Gas* (2020) arXiv:2010.15704 [hep-ph].
- [31] A. Nakamura and S. Sakai, Phys. Rev. Lett. **94**, 072305 (2005), arXiv:hep-lat/0406009.
- [32] H. B. Meyer, Phys. Rev. D **76**, 101701 (2007), arXiv:0704.1801 [hep-lat].
- [33] N. Astrakhantsev, V. Braguta, and A. Kotov, JHEP **04**, 101 (2017), arXiv:1701.02266 [hep-lat].
- [34] L. Altenkort, A. M. Eller, A. Francis, O. Kaczmarek, L. Mazur, G. D. Moore, and H.-T. Shu, Phys. Rev. D **108**, 014503 (2023), arXiv:2211.08230 [hep-lat].
- [35] I. A. Karpenko, P. Huovinen, H. Petersen, and M. Bleicher, Phys. Rev. C **91**, 064901 (2015), arXiv:1502.01978 [nucl-th].
- [36] C. Shen and U. Heinz, Nucl. Phys. News **25**, 6 (2015), arXiv:1507.01558 [nucl-th].
- [37] S. Ryu, J. F. Paquet, C. Shen, G. S. Denicol, B. Schenke, S. Jeon, and C. Gale, Phys. Rev. Lett. **115**, 132301 (2015), arXiv:1502.01675 [nucl-th].
- [38] B. Schenke, C. Shen, and P. Tribedy, Phys. Rev. C **99**, 044908 (2019), arXiv:1901.04378 [nucl-th].
- [39] S. Ryu, J.-F. Paquet, C. Shen, G. Denicol, B. Schenke, S. Jeon, and C. Gale, Phys. Rev. C **97**, 034910 (2018), arXiv:1704.04216 [nucl-th].
- [40] H. Niemi, K. J. Eskola, and R. Paatelainen, Phys. Rev. C **93**, 024907 (2016), arXiv:1505.02677 [hep-ph].
- [41] C. Shen and S. Alzhirani, Phys. Rev. C **102**, 014909 (2020), arXiv:2003.05852 [nucl-th].
- [42] C. Shen, Nucl. Phys. A **1005**, 121788 (2021), arXiv:2001.11858 [nucl-th].
- [43] P. F. Kolb, U. W. Heinz, P. Huovinen, K. J. Eskola, and K. Tuominen, Nucl. Phys. A **696**, 197 (2001), arXiv:hep-ph/0103234.
- [44] J. Bartels, K. J. Golec-Biernat, and H. Kowalski, Phys. Rev. D **66**, 014001 (2002), arXiv:hep-ph/0203258.
- [45] H. Kowalski and D. Teaney, Phys. Rev. D **68**, 114005 (2003), arXiv:hep-ph/0304189.
- [46] Z.-W. Lin, C. M. Ko, B.-A. Li, B. Zhang, and S. Pal, Phys. Rev. C **72**, 064901 (2005), arXiv:nucl-th/0411110.
- [47] T. Hirano, U. W. Heinz, D. Kharzeev, R. Lacey, and Y. Nara, Phys. Lett. B **636**, 299 (2006), arXiv:nucl-th/0511046.
- [48] H.-J. Drescher, A. Dumitru, A. Hayashigaki, and Y. Nara, Phys. Rev. C **74**, 044905 (2006), arXiv:nucl-th/0605012.
- [49] H.-J. Drescher and Y. Nara, Physical Review C **75** (2007), 10.1103/physrevc.75.034905.
- [50] H. Petersen, J. Steinheimer, G. Burau, M. Bleicher, and H. Stöcker, Phys. Rev. C **78**, 044901 (2008), arXiv:0806.1695 [nucl-th].
- [51] K. Werner, I. Karpenko, T. Pierog, M. Bleicher, and K. Mikhailov, Phys. Rev. C **82**, 044904 (2010), arXiv:1004.0805 [nucl-th].
- [52] A. Accardi *et al.*, Eur. Phys. J. A **52**, 268 (2016), arXiv:1212.1701 [nucl-ex].
- [53] B. Schenke, P. Tribedy, and R. Venugopalan, Phys. Rev. Lett. **108**, 252301 (2012), arXiv:1202.6646 [nucl-th].

- th].
- [54] M. Rybczynski, G. Stefanek, W. Broniowski, and P. Bozek, *Comput. Phys. Commun.* **185**, 1759 (2014), arXiv:1310.5475 [nucl-th].
- [55] J. S. Moreland, J. E. Bernhard, and S. A. Bass, *Phys. Rev. C* **92**, 011901 (2015), arXiv:1412.4708 [nucl-th].
- [56] W. van der Schee and B. Schenke, *Phys. Rev. C* **92**, 064907 (2015), arXiv:1507.08195 [nucl-th].
- [57] O. Garcia-Montero, H. Elfner, and S. Schlichting, (2023), arXiv:2308.11713 [hep-ph].
- [58] N. Götz, L. Constantin, and H. Elfner, (2023), arXiv:2312.05001 [nucl-th].
- [59] N. Götz and H. Elfner, *Phys. Rev. C* **106**, 054904 (2022), arXiv:2207.05778 [hep-ph].
- [60] S. Pratt, E. Sangaline, P. Sorensen, and H. Wang, *Phys. Rev. Lett.* **114**, 202301 (2015), arXiv:1501.04042 [nucl-th].
- [61] J. E. Bernhard, J. S. Moreland, S. A. Bass, J. Liu, and U. Heinz, *Phys. Rev. C* **94**, 024907 (2016), arXiv:1605.03954 [nucl-th].
- [62] J. Auvinen, J. E. Bernhard, S. A. Bass, and I. Karpenko, *Phys. Rev. C* **97**, 044905 (2018), arXiv:1706.03666 [hep-ph].
- [63] J. E. Bernhard, J. S. Moreland, and S. A. Bass, *Nature Phys.* **15**, 1113 (2019).
- [64] G. Nijs, W. van der Schee, U. Gürsoy, and R. Snellings, *Phys. Rev. Lett.* **126**, 202301 (2021), arXiv:2010.15130 [nucl-th].
- [65] D. Everett, W. Ke, J.-F. Paquet, G. Vujanovic, S. A. Bass, L. Du, C. Gale, M. Heffernan, U. Heinz, D. Liyanage, M. Luzum, A. Majumder, M. McNelis, C. Shen, Y. Xu, A. Angerami, S. Cao, Y. Chen, J. Coleman, L. Cunqueiro, T. Dai, R. Ehlers, H. Elfner, W. Fan, R. J. Fries, F. Garza, Y. He, B. V. Jacak, P. M. Jacobs, S. Jeon, B. Kim, M. Kordell, A. Kumar, S. Mak, J. Mulligan, C. Nattrass, D. Oliinychenko, C. Park, J. H. Putschke, G. Roland, B. Schenke, L. Schwiebert, A. Silva, C. Sirimanna, R. A. Soltz, Y. Tachibana, X.-N. Wang, and R. L. Wolpert (JETSCAPE Collaboration), *Phys. Rev. Lett.* **126**, 242301 (2021), arXiv:2010.03928 [hep-ph].
- [66] D. Everett, W. Ke, J.-F. Paquet, G. Vujanovic, S. A. Bass, L. Du, C. Gale, M. Heffernan, U. Heinz, D. Liyanage, M. Luzum, A. Majumder, M. McNelis, C. Shen, Y. Xu, A. Angerami, S. Cao, Y. Chen, J. Coleman, L. Cunqueiro, T. Dai, R. Ehlers, H. Elfner, W. Fan, R. J. Fries, F. Garza, Y. He, B. V. Jacak, P. M. Jacobs, S. Jeon, B. Kim, M. Kordell, A. Kumar, S. Mak, J. Mulligan, C. Nattrass, D. Oliinychenko, C. Park, J. H. Putschke, G. Roland, B. Schenke, L. Schwiebert, A. Silva, C. Sirimanna, R. A. Soltz, Y. Tachibana, X.-N. Wang, and R. L. Wolpert (JETSCAPE Collaboration), *Phys. Rev. C* **103**, 054904 (2021), arXiv:2011.01430 [hep-ph].
- [67] J. E. Parkkila, A. Onnerstad, S. F. Taghavi, C. Mordasini, A. Bilandzic, M. Virta, and D. J. Kim, *Phys. Lett. B* **835**, 137485 (2022), arXiv:2111.08145 [hep-ph].
- [68] J. E. Parkkila, A. Onnerstad, and D. J. Kim, *Phys. Rev. C* **104**, 054904 (2021), arXiv:2106.05019 [hep-ph].
- [69] D. R. Phillips *et al.*, *J. Phys. G* **48**, 072001 (2021), arXiv:2012.07704 [nucl-th].
- [70] M. R. Heffernan, C. Gale, S. Jeon, and J.-F. Paquet, *Phys. Rev. Lett.* **132**, 252301 (2024), arXiv:2306.09619 [nucl-th].
- [71] M. R. Heffernan, C. Gale, S. Jeon, and J.-F. Paquet, *Phys. Rev. C* **109**, 065207 (2024), arXiv:2302.09478 [nucl-th].
- [72] S. A. Jahan, H. Roch, and C. Shen, “Bayesian analysis of (3+1)d relativistic nuclear dynamics with the rhic beam energy scan data,” (2024), arXiv:2408.00537 [nucl-th].
- [73] C. Shen, B. Schenke, and W. Zhao, “Viscosities of the baryon-rich quark-gluon plasma from beam energy scan data,” (2023), arXiv:2310.10787 [nucl-th].
- [74] H. Roch, S. A. Jahan, and C. Shen, (2024), arXiv:2405.12019 [nucl-th].
- [75] <https://github.com/smash-transport/smash-vh11e-hybrid>.
- [76] J. Auvinen and H. Petersen, *Phys. Rev. C* **88**, 064908 (2013), arXiv:1310.1764 [nucl-th].
- [77] I. Karpenko, P. Huovinen, and M. Bleicher, *Comput. Phys. Commun.* **185**, 3016 (2014).
- [78] G. S. Denicol, S. Jeon, and C. Gale, *Phys. Rev. C* **90**, 024912 (2014).
- [79] S. Ryu, J.-F. Paquet, C. Shen, G. S. Denicol, B. Schenke, S. Jeon, and C. Gale, *Phys. Rev. Lett.* **115**, 132301 (2015).
- [80] J. Steinheimer, S. Schramm, and H. Stoecker, *Phys. Rev. C* **84**, 045208 (2011), arXiv:1108.2596 [hep-ph].
- [81] A. Motornenko, J. Steinheimer, V. Vovchenko, S. Schramm, and H. Stoecker, *Phys. Rev. C* **101**, 034904 (2020), arXiv:1905.00866 [hep-ph].
- [82] E. R. Most, A. Motornenko, J. Steinheimer, V. Dexheimer, M. Hanauske, L. Rezzolla, and H. Stoecker, *Phys. Rev. D* **107**, 043034 (2023), arXiv:2201.13150 [nucl-th].
- [83] P. Huovinen and H. Petersen, *Eur. Phys. J. A* **48** (2012), 10.1140/epja/i2012-12171-9.
- [84] <https://github.com/smash-transport/smash-hadron-sampler>.
- [85] F. Cooper, G. Frye, and E. Schonberg, *Phys. Rev. D* **11**, 192 (1975).
- [86] J. Weil, V. Steinberg, J. Staudenmaier, L. G. Pang, D. Oliinychenko, J. Mohs, M. Kretz, T. Kehrenberg, A. Goldschmidt, B. Bäuchle, J. Auvinen, M. Attems, and H. Petersen, *Phys. Rev. C* **94**, 054905 (2016).
- [87] D. Oliinychenko, V. Steinberg, J. Staudenmaier, J. Weil, A. Schäfer, H. E. (Petersen), S. Ryu, J. Mohs, F. Li, A. Sorensen, D. Mitrovic, L. Pang, void One, A. Sciarra, O. Garcia-Montero, M. Mayer, N. Kübler, and Nikita, “smash-transport/smash: SMASH-2.1,” (2021).
- [88] <https://smash-transport.github.io/>.
- [89] M. Tanabashi *et al.* (Particle Data Group), *Phys. Rev. D* **98**, 030001 (2018).
- [90] T. Sjöstrand, S. Mrenna, and P. Skands, **178**, 852 (2008).
- [91] J. Cleymans, H. Oeschler, K. Redlich, and S. Wheaton, *Phys. Rev. C* **73**, 034905 (2006), arXiv:hep-ph/0511094.
- [92] A. Andronic, P. Braun-Munzinger, and J. Stachel, *Nucl. Phys. A* **834**, 237C (2010), arXiv:0911.4931 [nucl-th].
- [93] L. Adamczyk *et al.* (STAR), *Phys. Rev. C* **96**, 044904 (2017), arXiv:1701.07065 [nucl-ex].
- [94] D. Neff (STAR), in *58th Rencontres de Moriond on QCD and High Energy Interactions* (2024) arXiv:2405.20928 [nucl-ex].
- [95] M. Molnár (STAR), *Universe* **9**, 335 (2023), arXiv:2307.14065 [nucl-ex].

- [96] O. Garcia-Montero, J. Staudenmaier, A. Schäfer, J. M. Torres-Rincon, and H. Elfner, Phys. Rev. C **105**, 064906 (2022), arXiv:2107.08812 [hep-ph].
- [97] B. I. Abelev *et al.* (STAR), Phys. Rev. C **79**, 034909 (2009), arXiv:0808.2041 [nucl-ex].
- [98] L. Adamczyk *et al.* (STAR), Phys. Rev. C **98**, 034918 (2018), arXiv:1701.06496 [nucl-ex].
- [99] L. Adamczyk *et al.* (STAR), Phys. Rev. Lett. **116**, 112302 (2016), arXiv:1601.01999 [nucl-ex].
- [100] B. B. Back *et al.* (PHOBOS), Phys. Rev. C **74**, 021902 (2006).
- [101] B. B. Back *et al.* (PHOBOS), Phys. Rev. C **72**, 051901 (2005), arXiv:nucl-ex/0407012.
- [102] <https://github.com/tisimst/pyDOE>.
- [103] J. L. Deutsch and C. V. Deutsch, Journal of Statistical Planning and Inference **142**, 763 (2012).
- [104] N. Sass, H. Roch, N. Götz, R. Krupczak, and C. B. Rosenkvist, (2025), arXiv:2503.09415 [physics.data-an].
- [105] H. Roch, N. Götz, N. Saß, and R. Krupczak, “smash-transport/sparkx: v2.0.2-chatelet,” (2025).
- [106] R. B. Gramacy, “Surrogates: Gaussian process modeling, design and optimization for the applied sciences,” (Chapman Hall/CRC, Boca Raton, Florida, 2020) <http://bobby.gramacy.com/surrogates/>.
- [107] C. E. Rasmussen, “Gaussian processes in machine learning,” in *Advanced Lectures on Machine Learning*, edited by O. Bousquet, U. von Luxburg, and G. Rätsch (Springer Berlin Heidelberg, Berlin, Heidelberg, 2004) pp. 63–71.
- [108] M. Plumlee, O. Sürer, S. M. Wild, and M. Y.-H. Chan, *surmise 0.3.0 Users Manual*, Tech. Rep. Version 0.3.0 (NAISE, 2024).
- [109] M. Karamanis, F. Beutler, J. A. Peacock, D. Nabergoj, and U. Seljak, Monthly Notices of the Royal Astronomical Society **516**, 1644 (2022).
- [110] M. Karamanis, D. Nabergoj, F. Beutler, J. A. Peacock, and U. Seljak, arXiv preprint arXiv:2207.05660 (2022).
- [111] T. Müller, B. McWilliams, F. Rousselle, M. Gross, and J. Novák, ACM Trans. Graph. **38** (2019), 10.1145/3341156.
- [112] N. Deutschmann and N. Götz, JHEP **03**, 083 (2024), arXiv:2401.09069 [hep-ph].
- [113] See Supplemental Material at [URL will be inserted by publisher] for raw data of all figures.